Syracuse University

SURFACE

Dissertations - ALL   SURFACE

12-2013

Precision measurement of the Lambda_b baryon lifetime

Bilas Kanti Pal

Follow this and additional works at: https://surface.syr.edu/etd

Part of the Physics Commons

Recommended Citation

Abstract

The ratio of the Λ_b^0 baryon lifetime to that of the $\overline{B}^0$ meson is measured using data corresponding to an integrated luminosity of 3.0 fb^{-1} collected with the LHCb detector using pp collisions at the LHC. The Λ_b^0 baryon is observed in the decay mode $\Lambda_b^0 \to J/\psi\, pK^-$, while the $\overline{B}^0$ meson decay used is the well known $\overline{B}^0 \to J/\psi\, \pi^+ K^-$ mode, where the $\pi^+ K^-$ mass is consistent with that of the $\overline{K}^{*0}(892)$ meson. The ratio of lifetimes is measured to be $0.971 \pm 0.007 \pm 0.005$, in agreement with theoretical expectations based on the heavy quark expansion. Using previous determinations of the $\overline{B}^0$ meson lifetime, the Λ_b^0 lifetime is found to be $1.476 \pm 0.010 \pm 0.010$ ps. In both cases the first uncertainty is statistical and the second systematic.

Precision measurement of the Λ_b^0 baryon lifetime

Dissertation

Submitted in Partial Fulfilment of the

Requirements of the degree of

Doctor of Philosophy

in Physics

by

Bilas Kanti Pal

MS, Syracuse University, Syracuse, NY, USA 2012

DICTP, The Abdus Salam ICTP, Trieste, Italy 2008

Department of Physics

Syracuse University

Syracuse, NY-13244

December 2013

To
My Mother

Acknowledgements

First and the foremost, I would like to thank my supervisor, Professor Sheldon Stone, who has been an excellent supervisor throughout. I feel fortunate to have had the opportunity to work with such a wonderful person and have guidance. His enduring enthusiasm is contagious and it really inspired me to push myself a bit further, develop my expertise in the field of my research. Without his support it would have been very difficult for me to carry this project to completion, and attain my most significant accomplishment to date.

I would also like to thank Liming Zhang who helped me over the years with everything from computing support to analysis advice. My heartiest thanks to all members of the high energy experimental group, Marina Artuso, Ray Mountain, Tomasz Skwarnicki, Steven Blusk, J. C. Wang and Mitchell Soderberg, who have provided me with much sound advice and guidance in my studies.

I specially acknowledge and thank the LHCb physics coordinator, Tim Gershon, the B2CC WG conveners, Stephanie Hansmann-Menzemer, Greig Cowan, Diego Martinez Santos and other members of the LHCb Collaboration, for their invaluable discussions and insightful suggestions throughout.

I thank my family for their endless support, love and encouragement, helping me pursue my interests in academics. Special thanks to my wife Harapriya and son Bisaj for their love and patient and giving me the courage to make it. Finally I thank all my wonderful friends and colleagues in Syracuse who made my stay here fun and memorable.

Declaration

This thesis is the result of my own work, except where explicit reference is made to the work of others, and has not been submitted for another qualification to this or any other university .

- Bilas Kanti Pal

Contents

List of Figures

List of Tables

Chapter 1

Introduction

Evaluations from experimental data of fundamental parameters, such as Cabibbo-Kobayashi-Maskawa (CKM) [1] matrix elements, and limits on physics beyond that described by the standard model, often rely on theoretical input [2]. One of the most useful models, the heavy quark expansion (HQE) [3–5], is used, for example, to extract values for $|V_{ub}|$ and $|V_{cb}|$ from measurements of inclusive semileptonic B meson decays [6]. An early prediction from this model was that the Λ_b^0 lifetime was almost equal to that of the $\overline{B}^0$ meson, but shorter by few percent [7–9]. Measurements from CERN's Large Electron-Positron (LEP) collider, however, indicated that $\tau_{\Lambda_b^0}/\tau_{\overline{B}^0}$ was lower. This caused concern over the applicability of HQE and various attempts were made to explain the observations. Recent measurements have indicated higher values but with relatively large uncertainties [10]. A most precise measurement of the Λ_b^0 baryon lifetime has recently been reported by LHCb [11] using a data sample corresponding to 1.0 fb^{-1} of integrated luminosity and lends substantial support to the HQE theory.

In this dissertation, we present the experimental determination of $\tau_{\Lambda_b^0}/\tau_{\overline{B}^0}$ with three times larger data than used previously. The Λ_b^0 baryon is detected in the $J/\psi\, pK^-$ decay mode, while the $\overline{B}^0$ meson is found in $J/\psi\, \overline{K}^{*0}(892)$ decays, with $\overline{K}^{*0}(892) \to \pi^+ K^-$. Mention of a particular decay channel implies the additional use of the charge-conjugate mode. The tree-level Feynman diagrams for the processes are shown in Fig. 1.1. These decays have the same decay topology into four charged tracks, thus facilitating the cancellation of systematic uncertainties in ratio. Here we present a precision measurement that demonstrates, in fact, that $\tau_{\Lambda_b^0}$ is quite similar to the $\overline{B}^0$ meson lifetimes.
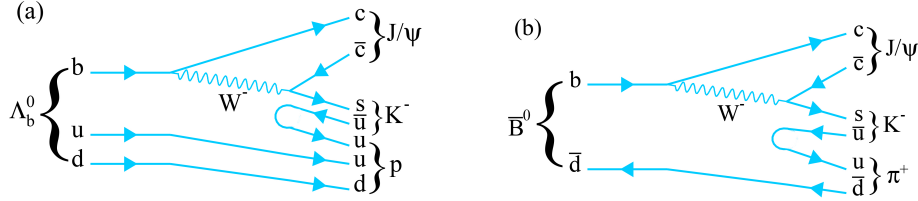
Figure 1.1: Leading order Feynman diagrams for (a) $\Lambda_b^0 \to J/\psi\, pK^-$ and (b) $\overline{B}^0 \to J/\psi\, \pi^+ K^-$ decay modes.

This dissertation is organized as follows: the theoretical framework and motivation for measuring the Λ_b^0 baryon lifetime are described in Chapter 2. Chapter 3 describes the summary of the LHCb experiment, used to collect the data analyzed for this measurement. Chapter 4 describes the reconstruction and selection of the desired events, while Chapter 5 introduces the fitting mechanism and describes the lifetime measurement. Possible systematic uncertainties on the measurement are investigated in Chapter 6. Finally, the results are presented in Chapter 7.

Chapter 2

Theoretical Overview

This chapter outlines the theoretical basis and the motivation of the study of Λ_b^0 lifetime. An overview of the "spectator model" of b hadron decays and the effects which lead to differences between the lifetimes of these particles are given. Then, a brief description of the heavy quark expansion (HQE) model and its prediction for the ratio of lifetimes are introduced.

2.1 Spectator model

A simple theoretical way to consider the decays of hadrons containing a heavy quark is the "spectator model", which states that only the heavy quark participates in the transition, while the light degrees of freedom are unaffected by the decay process. As a result, the model predicts that all the hadrons with the same heavy quark should have the same lifetime, regardless of the flavor of the accompanying quarks. The heavier the quark, the more valid the approximation. Under this assumption there is then a simple relation-
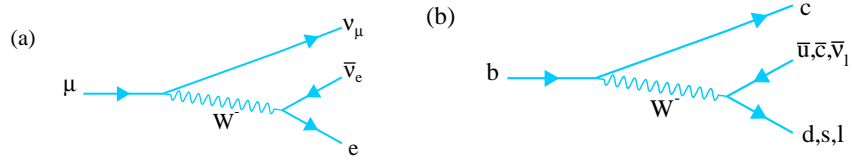
Figure 2.1: Feynman diagrams of (a) muon decay and (b) b quark decay.

ship between the decay width of b-flavored hadron and that of muon decay, illustrated in Fig. 2.1. For muon decay

$$\Gamma_\mu = \frac{G_F^2 m_\mu^5}{192\pi^3},\tag{2.1}$$

where m_μ is the mass of the muon and G_F is Fermi coupling constant, whilst for the decay of b-flavored hadron

$$\Gamma_b = \frac{9|V_{cb}|^2 G_F^2 m_b^5}{192\pi^3},\tag{2.2}$$

where m_b is the b-quark mass and V_{cb} is the CKM matrix element [1] for quark coupling (there is also a term with $|V_{ub}|^2$, which is small and has been neglected). In muon decay, the virtual W-boson decays to $e\bar{\nu}_e$, as it is the only kinematically allowed channel, whereas in b decays, W-boson can decay to any of the three lepton generations $(e\bar{\nu}_e, \mu\bar{\nu}_\mu, \tau\bar{\nu}_\tau)$ and the two quark generations $(u\bar{d}, c\bar{s})$, with three color combinations for the last two possibilities. Therefore, the phase space for the b decay is nine times larger than that of the muon decay. Furthermore, the quark-quark couplings and the mass of the decaying particle must be adjusted when starting from the muon decay formula. This gives

$$\tau_b = \frac{1}{\Gamma_b} \approx 1.3 - 1.7 \text{ ps},\tag{2.3}$$

4

with $m_b = 4.18 \pm 0.03$ GeV and $|V_{cb}| = (40.9 \pm 1.1) \times 10^{-3}$ [1], which is of the order of the observed b hadron lifetimes.

The spectator model predicts the equal lifetimes for all b hadron species. However, this assumption is too naïve, since effects of other quarks in the hadron are not taken into account. Therefore, a great deal of additional effort is needed to relate the b hadron lifetimes to the basic theory we have just outlined. In particular, the effects arising in the presence of a lighter quark must be taken into account.

The "spectator effects" involve the participation of the light constituents in the decay and thus contribute to the differences in the decay widths and lifetimes of different species of b-flavored hadrons. The main sources of such effects are Pauli Interference (PI), weak annihilation (WA) for mesons, and weak exchange (WE) for baryons [12].

2.2   Heavy Quark Expansion

The spectator effects can phenomenologically explain the origin of lifetime differences of different b-flavored hadrons. But it cannot make precise lifetime predictions. At present, one of the most useful theoretical approach for the study of the b hadron lifetimes is the Heavy Quark Expansion (HQE) [3–5]. Its technical foundation is the operator product expansion (OPE) [13].

HQE is a method to separate the non-perturbative, long-distance quantum chromodynamics (QCD) contributions to the decay amplitude from the short-distance electroweak contributions. In the framework of HQE, the total decay width of a b-flavored hadron can be expressed as an expansion in

5

inverse power of the b quark mass, $(1/m_b^n)$, as

$$\Gamma = \Gamma_0 \left[a_0 + a_2 \left(\frac{\Lambda_{QCD}}{m_b} \right)^2 + a_3 \left(\frac{\Lambda_{QCD}}{m_b} \right)^3 + \cdots \quad \cdots \quad \cdots \right], \qquad (2.4)$$

where Γ_0 is the term which describes the spectator model, $\Lambda_{QCD} \approx 200$ MeV is the QCD scale. The coefficients a_n are calculable coefficients.

The leading term of this expansion corresponds to the decay of a free b quark. This term is universal, contributing equally to the lifetimes of all b hadron species. No $\mathcal{O}(1/m_b)$ contributions can arise in OPE. At this order the decay proceeds as in the spectator model, with no interaction with the light spectator quark. The first correction to this expansion is of the order of $(1/m_b^2)$ [3–5]. At this order the Fermi motion of the b quark and interactions between its spin and that of the light degrees of freedom enter. This term is sensitive to lifetime differences between mesons and baryons. The difference is mainly driven by the fact that light quarks in Λ_b^0 baryon appear in a spin zero quantum state, decay more quickly than mesons that interact with a spin half antiquark cloud, which causes a shift of $(1-2)\%$ [8,9] in the ratio of Λ_b^0 and B^0 lifetimes. This leads to the theoretical [9] predictions of

$$
\begin{aligned}
\frac{\tau_{B^-}}{\tau_{B^0}} &= 1 + \mathcal{O}\left(1/m_b^3\right) \qquad (2.5) \\
\frac{\tau_{B_s^0}}{\tau_{B^0}} &= (1.00 \pm 0.01) + \mathcal{O}\left(1/m_b^3\right) \\
\frac{\tau_{\Lambda_b^0}}{\tau_{B^0}} &= 0.98 + \mathcal{O}\left(1/m_b^3\right)
\end{aligned}
$$

The term of $\mathcal{O}(1/m_b^3)$ reflects the spectator effects, whose contribution is additionally enhanced due to a factor $16\pi^2$ with respect to the leading free heavy quark. However, the effects of $\mathcal{O}(1/m_b^3)$ is estimated to be small [14].

6

In the past, experimental results, particularly for $\tau_{\Lambda_b^0}/\tau_{B^0}$, have been in disagreement with the theoretical expectations. In 2003 one widely quoted average of all data gave 0.798 ± 0.052 [15], while another gave 0.786 ± 0.034 [16]. Some authors sought to explain the small value of the ratio by including additional operators or other modifications [17], while some thought that the HQE could be pushed to provide a ratio of ~ 0.9 [18]. Recent measurements have shown indications that a higher value is possible [10], although the uncertainties are still large. This situation has recently been clarified by a precise LHCb measurement [11]. This dissertation reports even more precise measurement of the Λ_b^0 baryon lifetime than the previously published "precision measurement of the Λ_b^0 baryon lifetime" [11], where I also contributed too.

Chapter 3

The LHCb Experiment

This chapter begins with a brief description of the Large Hadron Collider and its various detectors. An explanation of the LHCb detector and its various hardware components and data acquisition system is then discussed. More detailed description of the LHCb detector can be found in Ref. [19].

3.1 The Large Hadron Collider

The Large Hadron Collider (LHC), located at the European Organization for Nuclear Research (CERN) is the world's highest energy particle accelerator. It is designed to collide two beams of protons at a center-of-mass energy, $\sqrt{s}$, up to 14 TeV, with a maximum instantaneous luminosity, $\mathcal{L}$, of 10^{34} cm^{-2} s^{-1}. The LHC occupies the same tunnel as its predecessor. It consists of a 27-kilometre ring of superconducting magnets with a number of accelerating structures to boost the energy of the particles along the way. The protons are injected from the Super Proton Synchrotron (SPS) into the main rings
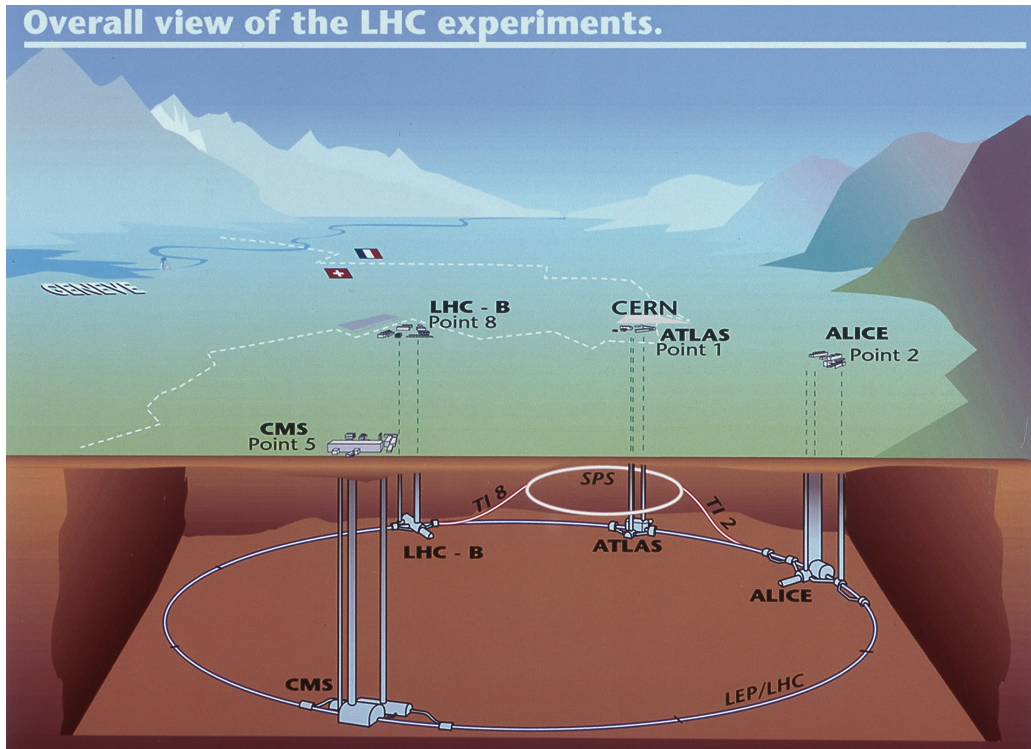
Figure 3.1: An overview of the LHC, showing the geographical location of the four main experiments.

with an energy of 450 MeV. To accelerate the beams to its design energy whilst keeping them in a stable orbit, a magnetic field strength of 8.3 teslas (T) is required. Proton beams are not continuous, but spaced in "bunches" of about 10^{11} protons each. The time separation between two adjacent bunches is a multiple of 25 ns, which corresponds to a bunch-crossing rate of 40 MHz.

Collisions between the two beams occur in four distinct points along the ring, where the detectors of the four major LHC experiments are installed. The ATLAS [20] and CMS [21] are general purpose experiments, mainly de-

signed to search for the Higgs boson and for direct evidence of physics beyond the Standard Model (SM). The ALICE [22] experiment is dedicated to the reconstruction of heavy ions collisions in order to study the formation of the quark-gluon plasma, a state of matter in which quarks and gluons are de-confined. Finally, the LHCb [19] experiment, in which this work took place, is designed for precision measurement of beauty and charm physics, specially the measurement of CP violation in this sector. A pictorial representation of the LHC is shown in Fig. 3.1.

3.2   The LHCb detector

The LHCb detector [19] is a single-arm spectrometer with forward angular momentum coverage from 10 mrad to 300 mrad in the bending plane and 10 mrad to 250 mrad in the non-bending plane. This corresponds to a pseudorapidity range of $1.8 < \eta < 4.9$, where $\eta = -\ln[\tan(\theta/2)]$, with θ being the polar angle with respect to the beam direction. This forward geometry utilises the fact that at LHC energies, the b-hadrons are predominantly produced in narrow angular cones in the forward and backward directions.

A schematic of the LHCb detector is shown in Fig. 3.2. The collisions take place in the far left in the VELO (VEtex LOcator). The interaction point of LHCb is displaced by 11.25 m from the center of the LHC optics to make optimal use of cavern space. Moving to the right there are the tracking systems (TT, T1, T2, and T3), two ring image Cherenkov detectors (RICH1 and RICH2), a dipole magnet, electromagnetic and hadronic calorimeters (ECAL and HCAL) and a muon detection system (M1-M5). These components are

now described in turn.
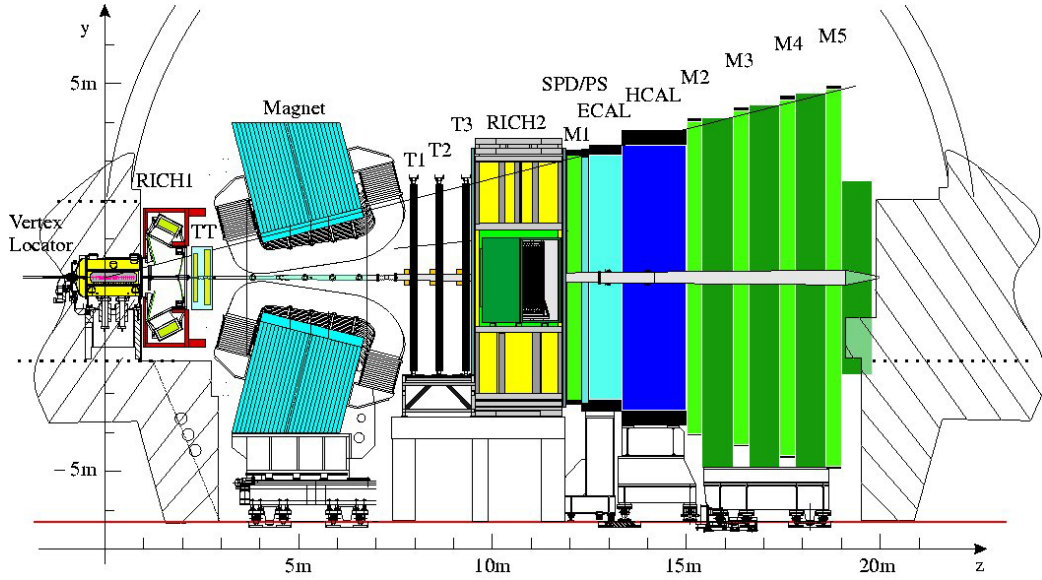
Figure 3.2: A schematic of the LHCb detector layout.

3.3   Luminosity levelling

LHCb is designed to run at a luminosity of 2×10^{32} cm^{-2}s^{-1}, which is below the luminosity at which ATLAS and CMS operate. To meet LHCb's requirements, a technique known as "luminosity levelling" is used. A machine setup is chosen that would give a peak luminosity well above the required maximum if the beams are collided head-on at LHCb's interaction point. This peak luminosity is then reduced to the required maximum by moving the two beams transversely apart at the interaction point. As the beam current goes

11

down during a fill,[1] the beams can be moved together in small increments to keep the collision rate constant throughout the fill.
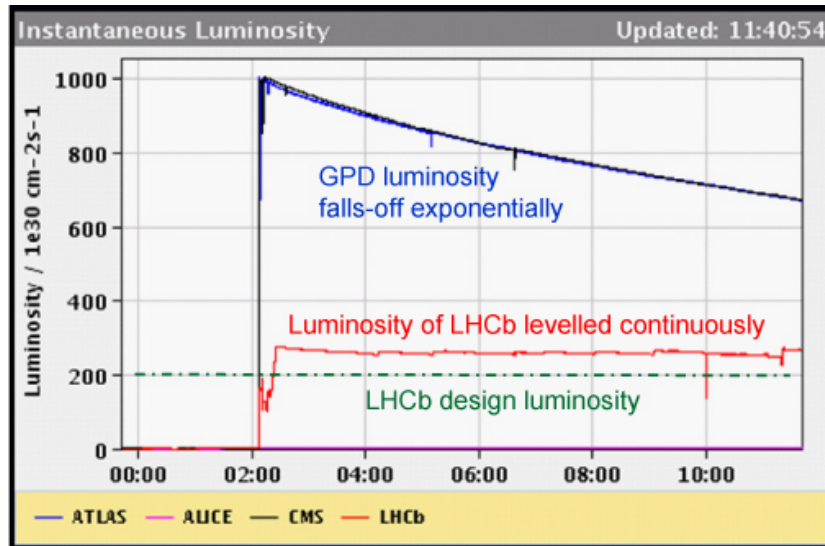
Figure 3.3: Example of a fill with luminosity levelling in LHCb. The observed near constant luminosity at LHCb is obtained through luminosity levelling.

Example of a fill with luminosity levelling in LHCb is shown in Fig. 3.3. The LHCb has an almost constant instantaneous luminosity, whereas the luminosity drops exponentially for ATLAS and CMS while the beams are being collided. Note also that, the maximum luminosity provided in 2012 has been around 4×10^{32} cm^{-2}s^{-1}, above its design luminosity.

---

[1]A fill is the name given to the time where the beams are colliding without being reinjected.

3.4 Tracking

The LHCb tracking system consists of the VELO, the dipole magnet, and four tracking stations; the TT, T1, T2 and T3. The TT is located between the VELO and the magnet, while the other trackers are found downstream of the magnet. The VELO and TT use silicon microstrip detectors. In T1−T3, the detectors are comprised of two distinct sections: the Inner Tracker (IT) in the region close to the beam pipe, and the Outer Tracker (OT) in the outer region of the trackers. Silicon microstrips are used in the IT, while straw-tubes are used in the OT.

3.4.1 VELO

The VELO [23] provides precise measurements of track coordinates close to the interaction region, which are used to identify the displaced secondary vertices that are a distinctive feature of b and c-flavored hadron decays. The VELO detector consists of 21 modules, positioned along the beam direction (see Fig. 3.4). In physics running conditions, the two modules are displaced from the beam pipe by 8 mm. In this position, the geometry is such that it allows the two halves of the VELO to overlap. This is to ensure that the sensors cover the full angular acceptance. The VELO sensors are placed at a radial distance of 3 cm from the beam, required by the LHC during injection in order to minimize radiation damage due to the unfocused beam.

Each module comprises two silicon strip sensors: the R-sensors and the ϕ-sensors. The R-sensors consists of a series of silicon strips oriented in concentric semi-circles with their centre at the nominal LHC beam position,

13
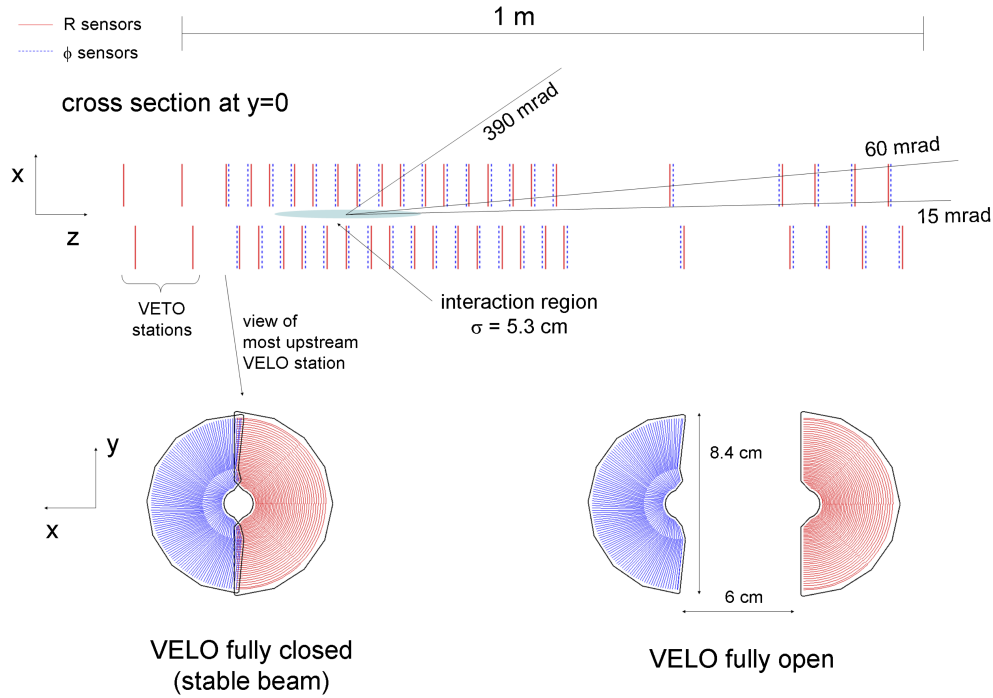
Figure 3.4: (above) Cross-section of the VELO in the magnet bending plane at $y = 0$. The modules are shown in the fully closed position. The two pile-up veto stations are indicated on the far left of the diagram. (below) The front face of the first module in both the closed and open positions.

allowing detection of the radial component of the tracks. On the other hand, the ϕ-sensors are distributed radially around the module in order to measure the position of the track in the ϕ direction. The z coordinate is obtained from the position of the module. The VELO uses a cylindrical coordinate system (R, ϕ, z), because it gives fast reconstruction of vertices and tracks in the LHCb trigger. Two planes perpendicular to the beam line and located upstream of the VELO sensors are called the "pile-up veto system" and are

14

used to determine the multiplicity of collisions.

The detectors are mounted in a vessel that maintains vacuum around the sensors and is separated from the machine vacuum by a thin walled corrugated aluminium sheet. This is done to minimize the material traversed by a charged particle before it crosses the sensors. The track definition within the LHCb acceptance $(1.8 < \eta < 4.9)$ requires hits in at least three VELO modules.

3.4.2   Silicon Tracker

The Silicon Tracker (ST) comprises two detectors: the Tracker Turicensis (TT)[2] [24] and the Inner Tracker (IT) [25]. Both TT and IT use silicon microstrip sensors with active surface areas of 8.4 m^2 and 4.0 m^2, respectively. The TT is located upstream of the LHCb dipole magnet and covers the full acceptance of the experiment. The IT covers a 120 cm wide and 40 cm high cross shaped region in the centre of the three tracking stations downstream of the magnet.

Each of the four ST stations has four detection layers in an $(x-u-v-x)$ arrangement with vertical strips in the first and the last layer and strips rotated by a stereo angle of $-5°$ and $+5°$ in the second and the third layer, respectively. This is illustrated in Fig. 3.5. The TT aims at reconstructing low momentum tracks that are swept out of the detector acceptance by the magnet and tracks that come from the decay of very long lived particles. The IT reconstructs tracks that passed through the magnetic field region and lie near the beam axis. Although IT covers only 1.3% of the region covered by

_____

[2]The Tracker Turicensis was formerly known as the Trigger Tracker.
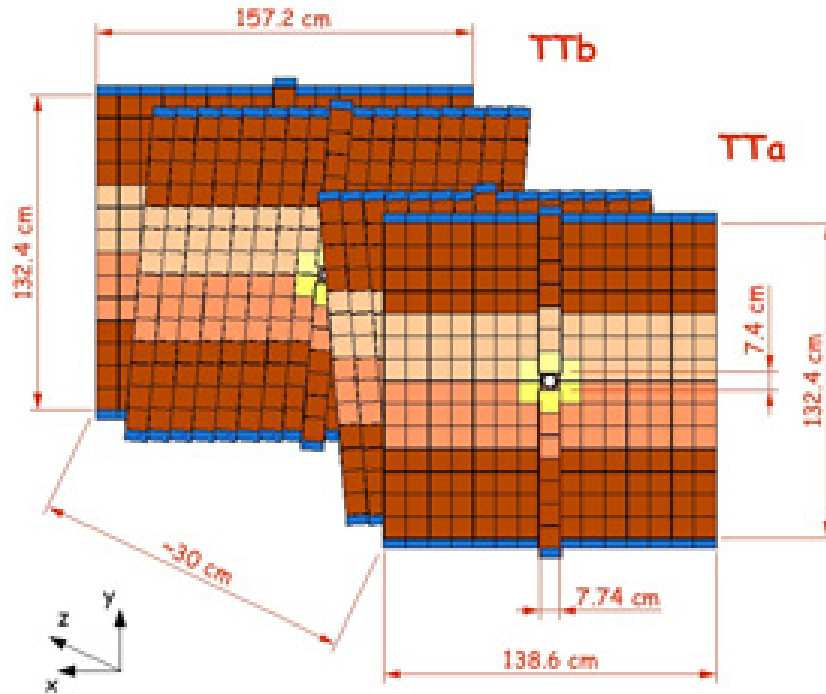
Figure 3.5: Schematic of the TT showing TTa at the front and TTb behind. Each layer is rotated slightly relative to its adjacent layer, known as $x - u - v - x$ geometry.

the tracking stations, approximately 20% of charged particles produced have their tracks in the IT region.

3.4.3 Outer Tracker

The LHCb Outer Tracker (OT) [26] is a drift time detector, for the tracking of charged particles and the measurement of their momentum over a large acceptance area. Excellent momentum resolution is necessary for a precise determination of the invariant mass of the reconstructed b hadrons: a mass

16

resolution of 10 MeV for the decay $B_s^0 \rightarrow D_s^- \pi^+$ translates into a required momentum resolution of $\delta p/p \approx 0.4\%$. The reconstruction of high multiplicity B decays demands a high tracking efficiency and at the same time a low fraction of wrongly reconstructed tracks: a track efficiency of 95% would result, for the decay $B_s^0 \rightarrow D_s^- \pi^+$, in an overall reconstruction efficiency of 80%.

The OT is designed as an array of individual, gas-tight straw-tube modules. Each module contains two staggered layers (monolayers) of drift tubes with inner diameters of 4.9 mm. A mixture of Argon (70%) and CO_2 (30%) is used in order to guarantee a fast drift time (< 50 ns), and a sufficient drift coordinate resolution of 200 μm. The detector modules are arranged in three stations. Each station consists of four layers, arranged in an $x - u - v - x$ geometry, similar to IT. The outer boundary corresponds to an acceptance of 300 mrad in the magnet bending plane and 250mrad in the non-bending plane. The inner cross-shaped boundary of the OT acceptance was determined by the requirement that occupancies should not exceed 10% at nominal LHCb luminosity.

3.4.4 Magnet

In common with almost all high energy experiments, a dipole magnet [27] is used in the LHCb experiment to measure the momentum of charged particles. The magnetic field is vertically orientated and the integrated magnetic field of the magnet is 4 Tm which gives a resolution of 0.4% for momenta up to 200 GeV. The polarity of the magnet is able to be reversed allowing studies of detector asymmetry, which could impact CP violation measurements.

3.5 Particle identification

Particle identification (PID) is a fundamental requirement for LHCb. It uses the combined outputs of the calorimeters, muon chambers and Ring Imaging Cherenkov Detectors (RICH) to assign a likelihood to be either a muon, electron, proton, pion, or kaon to each track.

3.5.1 RICH

It is essential for the goals of the experiment to separate pions from kaons in selected B hadron decays, in order to separate similar decays such as $B^0_{(s)} \rightarrow \pi^+\pi^-,\ K^\pm\pi^\mp,\ K^+K^-$. The RICH detectors [28] use the Cherenkov effect to identify charged particles. The Cherenkov effect is the fact that photons are emitted by a charged particle moving in a dielectric medium with a speed greater than the speed of light in that medium. The photons are emitted in a cone around the direction of the charged particle. The cone opening angle depends on the speed of the particle. Knowing the momentum (measured by the tracking system) and the speed of a particle, one has access to its mass and can then identify it. LHCb has two such detectors, RICH1 and RICH2. RICH1 is located upstream of the magnet in the region between the VELO and the TT. It uses silica aereogel and C_4F_{10} and allows charged particle identification for momenta between 1 and 60 GeV. It covers polar angles from 25 to 300 mrad in the bending plane and to 250 mrad in the non bending plane. RICH2 is situated downstream of the magnet, after T3, and covers polar angles from 15 mrad to 120 mrad in the bending plane and to 100 mrad in the non bending plane. It uses CF_4 as dielectric medium and its
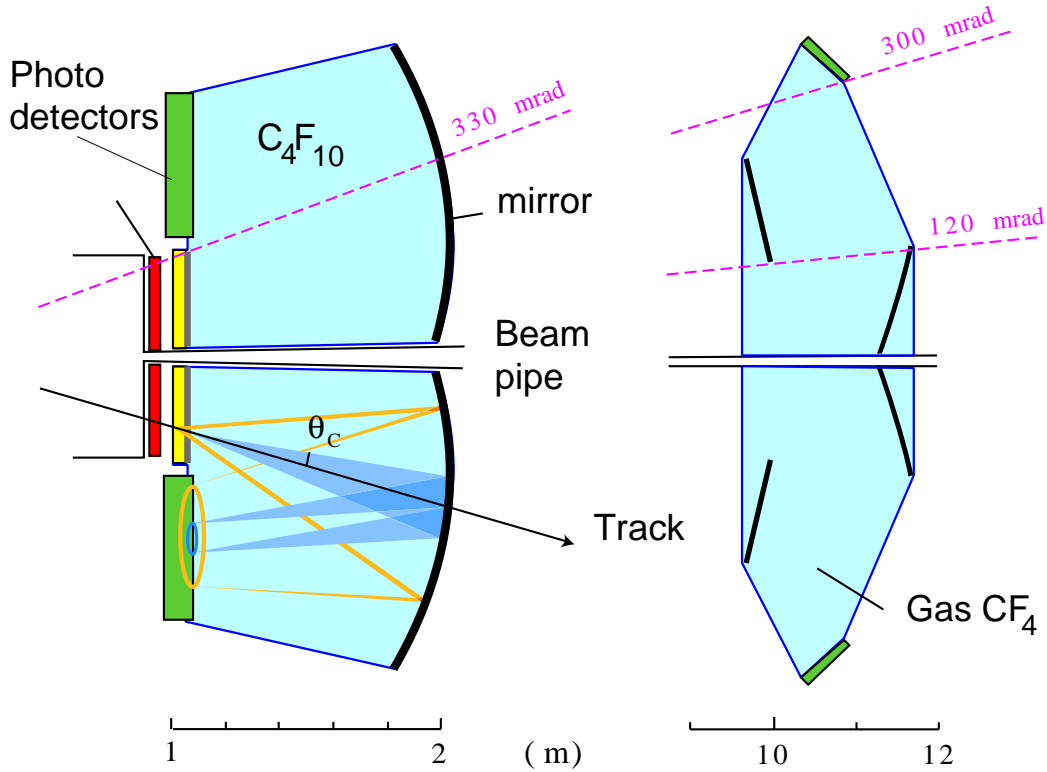
Figure 3.6: Schematic diagrams of (left) RICH1 and (right) RICH2 detectors.

momentum coverage goes from 15 GeV to 100 GeV. The schematic diagrams of both RICH detectors are shown in Fig. 3.6.

In both RICH detectors the focusing of the Cherenkov light is accomplished using a combination of spherical and flat mirrors to reflect the image out of the spectrometer acceptance. In the RICH1 the optical layout is vertical, whereas in RICH2, it is horizontal. Hybrid Photon Detectors (HPDs) are used to detect the Cherenkov photons in the wavelength range 200-600 nm. The HPDs are surrounded by external iron shields and are placed in MuMetal cylinders to permit operation in magnetic fields up to 50 mT.

3.5.2 Calorimeters

The calorimeter system performs multiple functions in LHCb. It selects transverse energy hadron, electron and photon candidates for the first trigger level (L0), which makes a decision 4 μs after the interaction. It provides the identification of electrons, photons and hadrons as well as the measurement of their energies and positions. The reconstruction with good accuracy of π^0 and prompt photons is essential for flavor tagging and for the study of B meson decays.

The LHCb calorimeter [29] system is located between the first and the second muon stations. The detectors which make up the calorimeters are all comprised of cells which increase in size with distance from the beam and reduction in particle flux. The calorimeter has four main parts: a scintillating pad detector (SPD); a pre-shower (PS); an electromagnetic calorimeter (ECAL); and a hadronic calorimeter (HCAL).

All calorimeters follow the same basic principle: scintillation light is transmitted to a Photo-Multiplier (PMT) by wavelength-shifting (WLS) fibres. The single fibres for the SPD/PS cells are read out using multianode photomultiplier tubes (MAPMT), while the fibre bunches in the ECAL and HCAL modules require individual phototubes.

The SPD/PS detector consists of a 15 mm, 2.5 radiation length thick, lead converter sandwiched between two almost identical planes of rectangular scintillator pads of high granularity. As no shower is initiated before the SPD, it will only detect charged tracks, while an electromagnetic shower can be initiated in the lead converter and subsequently detected in the PS. Thus the background from neutral pions can be suppressed by searching for hits

in the SPD, while the PS also suppresses the background of charged pions by requiring a shower profile at two segmented points along the beam axis.

The ECAL and HCAL, both are sampling calorimeters. The ECAL is located directly behind the SPD/PS system and records the rest of the electromagnetic shower. Layers of 4 mm thick scintillator and 2 mm lead are alternated over 42 cm, so that an electromagnetic shower is contained within the ECAL. The HCAL is located behind the ECAL detector. It utilises much thicker absorber layers (16 mm iron). The energy resolution given for each of the calorimeters is:

$$\frac{\sigma_E}{E}\big|_{ECAL} = \frac{10\%}{\sqrt{E}} \oplus 1\% \quad \text{and} \quad \frac{\sigma_E}{E}\big|_{HCAL} = \frac{(69 \pm 5)\%}{\sqrt{E}} \oplus (9 \pm 2)\%, \quad (3.1)$$

where energy is expressed in GeV.

3.5.3 Muon system

Muon triggering and offline muon identification are fundamental requirements of the LHCb experiment. Muons are present in the final states of many CP-sensitive B decays, in particular the two gold-plated decays, $B^0 \rightarrow J/\psi (\rightarrow \mu^+\mu^-)K_S^0$ and $B_s^0 \rightarrow J/\psi (\rightarrow \mu^+\mu^-)\phi$. These decay modes play an important role in CP asymmetry and oscillation measurements, since muon from semileptonic b decays provide a tag of the initial state falvor of the accompanying neutral b mesons. In addition, the study of rare b decays such as the falvor changing neutral current decay, $B_s^0 \rightarrow \mu^+\mu^-$, may reveal new physics beyond the Standard Model.

Muons are extremely penetrating and therefore muon chambers are installed at the end of the detector, where all other possible charged particles
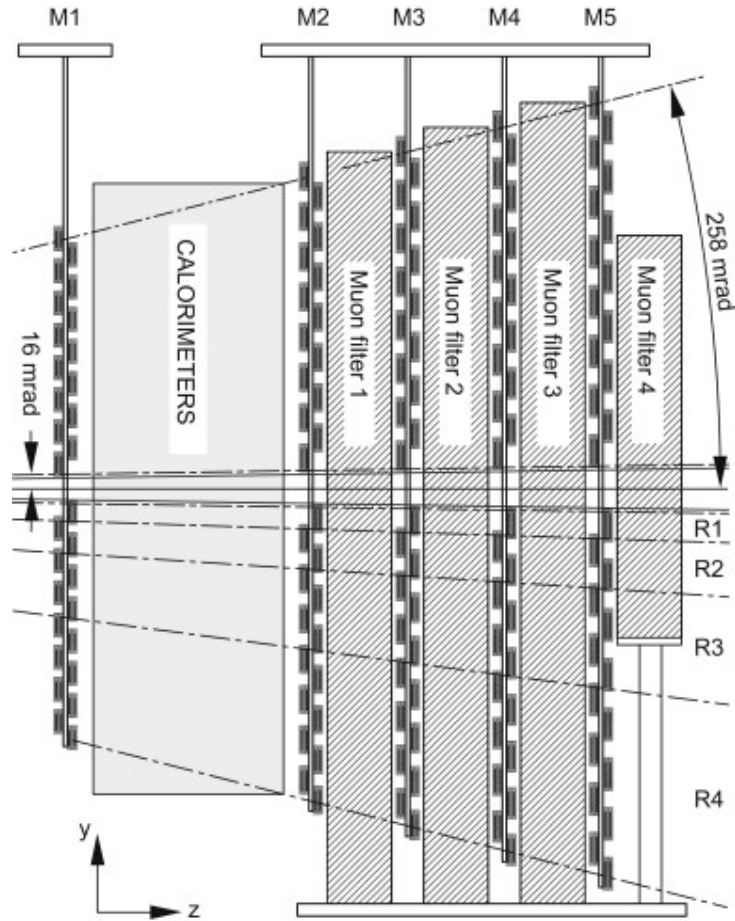
Figure 3.7: A schematic diagram of the muon system, with five stations indicated.

have been filtered. The muon system [30], shown in Fig. 3.7, is composed of five stations (M1-M5) of rectangular shape, placed along the beam axis, with a total of 1380 chambers covering a total area of 435 m^2. The inner and outer angular acceptances of the muon system are 20 (16) mrad and 306 (258) mrad in the bending (non-bending) plane, respectively, which roughly corresponds to a 20% acceptance of muons from semileptonic b decays. Station M1 is placed in front of the calorimeters and is used to improve the

p_T measurement in the trigger. The stations M2-M5 are placed downstream of the calorimeters and and are interleaved with 80 cm thick iron absorbers that select penetrating muons. The minimum momentum of a muon to cross the five stations is approximately 6 GeV since the total absorber thickness, including the calorimeters, is approximately 20 interaction lengths.

The muon trigger is based on stand-alone muon track reconstruction and p_T measurement and requires aligned hits in all five stations. Stations M1-M3 have a high spatial resolution in the bending plane and are used to define the track direction and calculate the p_T of the muon with a resolution of 20%. Stations M4 and M5 have a limited spatial resolution, their main purpose being the identification of penetrating particles.

Each Muon Station is divided into four regions, R1 to R4 with increasing distance from the beam axis. The linear dimensions of the regions R1, R2, R3, R4, and their segmentations scale in the ratio 1:2:4:8. With this geometry, the particle flux and channel occupancy are expected to be roughly the same over the four regions of a given station.

Multi-wire proportional chambers (MWPC) are used for all regions except the inner region of station M1 where the expected particle rate exceeds safety limits for ageing. The innermost region of M1 station comprises a series of three Gas Electron Multiplier (GEM) foils sandwiched between anode and cathode planes. MWPC and GEM both consist of a series of gas chambers across which a potential difference of several kV is applied. As particle traverses each chamber the gas is ionized and the subsequent charge avalanche is proportional to the signal.
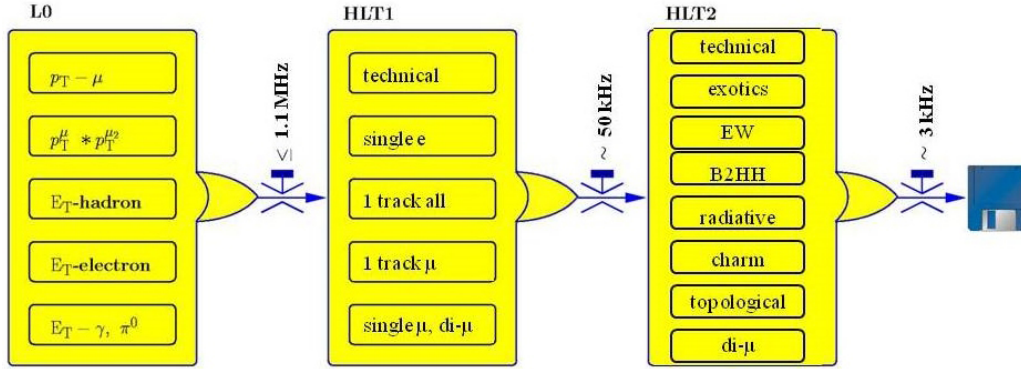
Figure 3.8: A flow diagram of the LHCb trigger sequences. The various stages and associated triggers are indicated, as well as the approximate event rate at each stage.

3.6 Trigger system

The LHCb experiment is designed to operate at an average luminosity of 2×10^{32} cm^{-2} s^{-1}, much lower than the maximum design luminosity of the LHC, reducing the radiation damage to the detectors and front-end electronics. At this luminosity the number of interactions per bunch crossing is dominated by single interactions, which facilitates the triggering and reconstruction by assuming low channel occupancy. With the LHC running under design conditions, the initial visible interactions in the LHCb are at a rate of 10 MHz. This is then reduced by a two stage trigger to about 2-3 kHz, at which rate the events are written to storage for further offline analysis. This reduction is achieved initially by the Level-0 (L0) hardware trigger, followed by the High Level Trigger (HLT). The schematic of the overall LHCb trigger scheme is shown in the Fig. 3.8 [31].

The purpose of the L0 trigger is to reduce the LHC beam crossing rate

of 40 MHz to the rate of 1 MHz with which the entire detector can be read out. The L0 information is coming from the pile-up sensors of the VELO, the calorimeters and the muon system. It is then sent to the Level-0 Decision Unit (L0DU), where the L0 selection algorithms are run.

The pile-up system has been implemented to reject events with a high number of primary vertices. The calorimeter trigger system looks for high transverse energy (E_T) leptons, hadrons and photons. It forms cluster by adding the E_T of 2×2 cells and selecting the clusters with the largest E_T. Clusters are identified as lepton, photon or hadron based on the information from the SPD, PS, ECAL and HCAL. The E_T of all HCAL cells is summed to reject crossings without visible interactions and to reject triggers on muon from the halo. The total number of hits in the SPD cells are counted to provide a measure of the charged track multiplicity in the crossing.

The muon chambers allow a stand-alone muon reconstruction with a p_T resolution of $\sim 20\%$. Track finding is performed by processing elements which combine the strip and pad data from the five muon stations to form towers pointing towards the interaction region. The muon stations are divided into quadrants and there is no exchange of information between the quadrants. In each quadrant, the two muon candidates with highest p_T are selected.

The HLT is the second level of LHCb trigger, running on events passing the L0 trigger. It consists of a C++ application which runs in several copies on every CPU of the Event Filter Farm (EFF), which consists of approximatively 1000 multi-core computing nodes. Currently there are 26110 copies of the application running in the EFF. The HLT application has access to all data in one event and thus, in principle, could execute the offline selection

algorithms. The HLT reduces the 1 MHz rate from the L0 to 2-3 kHz. The HLT is divided into two stages, HLT1 and HLT2.

HLT1 reduces the rate from the 1 MHz output of L0 to ~ 50 kHz. HLT1 reconstructs particles in the VELO and determines the position of the primary vertices (PV) in the event. To limit the CPU consumption, a selection of VELO tracks is made based on their smallest impact parameter (IP) to any PV, and their quality. For these selected VELO tracks their track-segment in the T-stations are sought to determine their momentum (p), so-called forward tracking. HLT1 selects events with at least one track which satisfies minimum requirements in IP, p, p_{T} and track quality. It reduces the rate to a sufficiently low level to allow forward tracking of all VELO tracks.

HLT2 searches for secondary vertices, and applies decay length and mass cuts to reduce the rate to the level at which the events can be written to storage and processed offline. Currently this is ~ 3 kHz. It first performs a complete pattern recognition to find all particle tracks in the event, using VELO tracks as seeds. Then, a set of different selections are applied. HLT2 runs exclusive and inclusive selections. The aim of the inclusive selection is to search for generic B decay features such as displaced vertices or dilepton pairs, while the exclusive selection aims to provide the highest possible efficiency on specific B decay channels.

3.7 LHCb computing

The LHCb core software is based in the GAUDI framework [32]. This framework is a well-structured C++ object-oriented architecture providing the

general needs of the LHCb software components. The simulation package is called GAUSS [33]. PYTHIA [34] with a configuration specific to LHCb detector is used to generate the proton-proton collisions [35]. The decays of hadronic particle are described by the EVTGEN package [36] in which PHOTOS [37] is used to generate final state radiations. GAUSS then communicates the output of PYTHIA as input of GEANT4 [38] which implements the interaction of the particles with the detector and the response of the active materials. The simulation of the digitization of the signals produced in the active materials is performed by the BOOLE package. It includes simulation of the readout electronics as well as of the L0 hardware trigger. The simulation output is digitized data that mimics the real data coming from the detector.

The event reconstruction is performed by the BRUNEL package. The MOORE application can be used to run the HLT selection on reconstructed events. This is especially useful to emulate the HLT response on the simulated data. The final stage of reconstruction is performed by the physics analysis software package DAVINCI. DAVINCI comprises the analysis and selection tools, such as particle identification algorithms, vertex fitting functions. It is also responsible of the administration and running of the *stripping*, a process in which events are further selected for physical analyses.

Chapter 4

Event selection and b hadron reconstruction

This chapter describes the selection and reconstruction of the data samples used in this analysis. The signal yields are then obtained by fitting the reconstructed b hadrons.

4.1 Event selection

The data sample contains 3.0 fb^{-1} of integrated luminosity collected with the LHCb detector [19] using pp collisions. One third of the data was acquired at a center-of-mass energy of 7 TeV, and the remainder at 8 TeV. Events are stored only if they satisfy certain criteria called collectively "the trigger". Events selected for this analysis are triggered by a $J/\psi \to \mu^+\mu^-$ decay, where the J/ψ is required at the software level to be consistent with coming from the decay of a b hadron by use either of IP

requirements or detachment of the J/ψ from the associated primary vertex. In particular, we select the events using the sample provided by the triggers `J_psi_1SHlt1Global_TOS` and `J_psi_1SHlt2Global_TOS`. Events used for this analysis are those from `Reco 14 stripping 20r1 Data` for 2011 data and `Reco 14 stripping 20 Data` for 2012 data and pass the `StrippingFullDSTDiMuonJpsi2MuMuDetachedLine` stripping line. The list of selections in this stripping line are given in Table 4.1.

Table 4.1: Selection requirements for the stripping line.

#	Selection variable	Requirement
1	$p_{\rm T}$ of muon	> 550 MeV
2	Muon PID	$\mathrm{DLL}(\mu - \pi) > 0$
3	Muon tracks χ^2/ndf	< 5
4	Muon $\chi^2_{\rm IP}$	> 4
5	J/ψ vertex χ^2	< 20
6	J/ψ mass window	$|m(\mu^+\mu^-) - m(J/\psi)| < 100$ MeV
7	J/ψ Flight distance significance	> 3

Event pre-selection requirements are based on previous Monte Carlo simulation as reported in Ref. [39]. We first implement the pre-selection that preserves a large fraction of the signal events. Table 4.2 summarizes the individual pre-selection requirements. Note that, the pre-selections are developed without applying cuts that can bias the b hadron lifetime, $i.e.$, no cuts are applied on $\chi^2_{\rm IP}$ of proton and kaon and flight distance and pointing angle of Λ_b^0.

Events satisfying this pre-selection are then further filtered using a mul-

Table 4.2: Analysis pre-selection requirements

#	Selection variables	Requirements
1	All tracks χ^2/ndf	< 4
2	p_{T} of muon	> 550 MeV
3	p_{T} of p and K^-	> 250 MeV
4	J/ψ vertex χ^2	< 16
5	J/ψ mass window	-48 to $+43$ MeV
6	Kaon PID	$\mathrm{DLL}(K - \pi) > 4$ & $\mathrm{DLL}(K - p) > -3$
7	Proton PID	$\mathrm{DLL}(p - \pi) > 10$ & $\mathrm{DLL}(p - K) > -3$
8	pK^- vertex χ^2	< 10
9	p_{T} of pK^-	> 1 GeV
10	Λ_b^0 χ^2_{IP}	< 25
11	Λ_b^0 Vertex χ^2	< 50
12	Λ_b^0 Decay time	> 0.2 ps
13	Ghost probability of kaon and proton	< 0.2
14	Trigger	Global Hlt1 & Hlt2 TOS on J/ψ
15	Clone track rejection	CloneDist≤ 0

tivariate analyzer based on a Boosted Decision Tree (BDT) technique [40]. The BDT uses seven variables that are chosen not to introduce an asymmetry between the two muons and provides a separation of signal and background. The BDT variables are the minimum DLL($\mu - \pi$) of the μ^+ and μ^- candidates (mmPIDmu); the $p_{\rm T}$ of p (pPT), K^- (KPT), pK^- combination (RPT) and Λ_b^0 (LPT); the Λ_b^0 vertex χ^2 (LCHI2) and the IP χ^2 of Λ_b^0 (LipCHI2). These variables are chosen with the aim of having the selection efficiency be independent of decay time.

The BDT technique involves a "training" procedure for event selection. A simulated signal and sideband data background samples are first used to train the selection. Then separate samples are used to test the BDT performance. We use 5×10^6 $\Lambda_b^0 \to J/\psi\, pK^-$ events that are generated uniformly in phase space with $J/\psi \to \mu^+\mu^-$ in the LHCb acceptance, using PYTHIA [34] with special LHCb parameter tune [35], and the LHCb detector simulation based on GEANT4 [38] described in Ref. [33]. A similar number of $\overline{B}^0 \to J/\psi\, \overline{K}^{*0}(892)$ events are also generated for other purposes.

To implement the BDT analysis technique, the simulated sample after the pre-selection is divided into two nearly equal parts, even and odd number of events that are grouped into sample A and sample B, respectively. We use sample A for the BDT training and then sample B to test the BDT performance. Half of the sideband events with $m(J/\psi\, pK^-)$ in the interval between 100 to 200 MeV below the Λ_b^0 mass in the 2012 data are used as a training sample, while the test sample uses the remaining half.[1] Signal and

---

[1]We choose not to use the upper sideband as it contains a higher fraction of reflections from $\overline{B}_s^0$ and $\overline{B}^0$ decays (see Fig. 4.6)

31

background distributions for each of the variables used in the BDT are shown in Fig. 4.1. There is discrimination power between signal and background in all of these variables.

The distributions of the BDT classifier output for signal and background is shown in Fig. 4.2. The b hadron candidates are further required to have a decay time higher than 0.4 ps to remove the large combinatorial background due to prompt J/ψ production. Final selections are determined by optimizing the detection sensitivities (Signal/$\sqrt{\text{Signal} + \text{Background}}$), by requiring BDT classifier output greater than 0.02. The numbers of signal and background events for BDT optimization are determined by fitting the $J/\psi\,pK^-$ mass spectrum in data for different values of the BDT cut.

4.2   The $\Lambda_b^0 \to J/\psi\,pK^-$ signal

The Λ_b^0 candidate invariant mass distribution is shown in Fig. 4.3. Candidate $\mu^+\mu^-$ combinations are constrained to the J/ψ mass for subsequent use in event selection; for determination of the lifetime, this procedure is not used. The vertical lines indicate the signal and sideband regions, where the signal region extends to ± 20 MeV around the Λ_b^0 mass peak and the sidebands extend from 60 MeV to 200 MeV on either side of the peak.

The Λ_b^0 candidate mass distribution can be polluted by reflections from other B meson decays where the particle identification fails. In particular, we need to estimate the size of the reflections from $\overline{B}_s^0 \to J/\psi\,K^+K^-$ where a kaon is misidentified as a proton and from $\overline{B}^0 \to J/\psi\,\overline{K}^{*0}(892)$ with $\overline{K}^{*0}(892) \to \pi^+K^-$ where the pion is misidentified as a proton. We proceed

by examining mass combinations in the sideband regions $60 - 200$ MeV on either side of the Λ_b^0 mass peak. Specifically, we take each of the candidates in the $J/\psi pK^-$ sideband regions, reassign proton to kaon and pion mass hypotheses, respectively and plot them separately. In doing so, the J/ψ mass is constrained to its nominal value [1]. The resulting distributions are shown in Fig. 4.4.

The $m(J/\psi K^+ K^-)$ distribution shows a large peak at the $\overline{B}_s^0$ mass. There is also a small contribution from the $\overline{B}^0$ final state where the π^+ is misidentified as a K^+ and the K^- as a $\overline{p}$, and then final state is interpreted as $J/\psi K^+ K^-$. The positions and shapes of the different contributions are determined by the simulation. We find the number of $\overline{B}_s^0$ events in the Λ_b^0 sideband by fitting the $m(J/\psi K^+ K^-)$ distribution in Fig. 4.4(a) with Gaussian signal function centered at the $\overline{B}_s^0$ mass, a polynomial background function and a shape imported from the simulation for the $\overline{B}^0$ double misidentification. There are $18\,039 \pm 183$ $\overline{B}_s^0$ and 5121 ± 277 $\overline{B}^0$ candidates in the Λ_b^0 sideband region. The $m(J/\psi \pi^+ K^-)$ distribution, on the other hand, shows a peak at the $\overline{B}^0$ mass with a large contribution from the $\overline{B}_s^0$ final state where the K^+ is misidentified as a π^+ and the K^- as a $\overline{p}$. The number of $\overline{B}^0$ events in the Λ_b^0 sideband are found by fitting the $m(J/\psi \pi^+ K^-)$ distribution in Fig. 4.4(b) with a signal Gaussian function at the $\overline{B}^0$ mass, a shape studied from simulation to describe the $\overline{B}_s^0$ double misidentification reflection (see also Section 4.4), and a polynomial function for the remaining background. We find 5474 ± 234 $\overline{B}^0$ candidates together with $18\,477 \pm 296$ $\overline{B}_s^0$ candidates. These numbers, in principle, should be the same as they are studied from the same sample of events. We use the average of the numbers obtained from

33

the two fits for the subsequent analysis.

We use simulations of the $\overline{B}_s^0 \to J/\psi\, K^+K^-$ and $\overline{B}^0 \to J/\psi\, K^-\pi^+$ decays to find the shape and normalization of these reflected backgrounds. The simulation of $\overline{B}_s^0 \to J/\psi\, K^+K^-$ is weighted to conform the results of our Dalitz plot analysis [41] in both decay angles and K^+K^- mass. For the simulation of $\overline{B}^0 \to J/\psi\, K^-\pi^+$, we use the dominant $\overline{K}^{*0}(892)$ component. (In the previous analysis [11], it has been checked by adding a $\overline{K}_2^*(1430)$ component and found no discernible difference.) Using the event yields found in data and the simulation shapes, we derive 5293 ± 86 $J/\psi\, K^+K^-$ reflection candidates within ± 20 MeV of Λ_b^0 peak. Similarly, 1087 ± 57 $J/\psi\,\pi^+K^-$ reflection candidates are calculated within ± 20 MeV of Λ_b^0 peak. These numbers are calculated as,

$$
\begin{aligned}
&\text{Expected number in } \pm 20 \text{ MeV} = \\
&\left(\frac{\text{Number of events within } \pm 20 \text{ MeV of } \Lambda_b^0 \text{ from simulation}}{\text{Number of events in } \Lambda_b^0 \text{ sideband regions from simulation}} \right) \times \\
&\text{(average number of events obtained from the } \overline{B}_s^0 \text{ and } \overline{B}^0 \text{ signal} \\
&\text{peaks shown in Fig. 4.4(a) and 4.4(b), respectively).}
\end{aligned}
\tag{4.1}
$$

Similarly, the expected numbers in the Λ_b^0 fit region ($[5500,5750]$ MeV) are calculated as,

$$
\begin{aligned}
&\text{Expected number in the fit region} = \\
&\left(\frac{\text{Number of events in the fit region of } \Lambda_b^0 \text{ from simulation}}{\text{Number of events in } \Lambda_b^0 \text{ sideband regions from simulation}} \right) \times \\
&\text{(average number of events obtained from the } \overline{B}_s^0 \text{ and } \overline{B}^0 \text{ signal} \\
&\text{peaks shown in Fig. 4.4(a) and 4.4(b), respectively),}
\end{aligned}
\tag{4.2}
$$

and are used as Gaussian constraints in the mass fit described below with the

central values as the Gaussian means and the uncertainties as the widths.

In addition, we have checked the possibility of double misidentification of $\Lambda_b^0 \to J/\psi\, pK^-$ with the proton and kaon mass swapped, and then interpreted as $J/\psi\, K^+ \overline{p}$. The resulting distribution is shown in Fig. 4.5. The distribution shows a peak at the Λ_b^0 mass. The resulting peak has 3194 ± 138 candidates, determined by the fit. Using the simulation of $\Lambda_b^0 \to J/\psi\, pK^-$ with the proton and kaon mass swapped, we calculate 1073 ± 46 double misidentified Λ_b^0 candidates under the Λ_b^0 peak. This number is also used as a Gaussian constraint in the mass fit.

To determine the number of Λ_b^0 signal candidates we perform an unbinned maximum likelihood fit to the candidate $J/\psi\, pK^-$ invariant mass spectrum shown in Fig. 4.6 (linear plot) and Fig. 4.7 (log plot). The fit function is the sum of the Λ_b^0 signal component, combinatorial background, the contributions from the $\overline{B}_s^0 \to J/\psi\, K^+K^-$ and $\overline{B}^0 \to J/\psi\, \pi^+K^-$ reflections and the double misidentified $J/\psi\, K^+ \overline{p}$, where the kaon and proton masses are swapped. The signal is modeled by a triple-Gaussian function with common mean. The fraction and the width ratio for the third Gaussian are fixed to that obtained in the fit $\overline{B}^0 \to J/\psi\, \overline{K}^{*0}(892)$, found in Refs. [11]. The effective r.m.s. width is 4.8 MeV. The combinatorial background is described by an exponential function. The shapes of the reflections and double misidentified contributions are described by histograms imported from the simulations. The mass fit gives $50\,379 \pm 335$ signal and $17\,126 \pm 103$ combinatorial background candidates together with 5350 ± 85 $\overline{B}_s^0 \to J/\psi\, K^+K^-$ and 1105 ± 57 $\overline{B}^0 \to J/\psi\, \pi^+K^-$ reflection candidates and 1039 ± 47 double misidentified Λ_b^0 candidates within ± 20 MeV of the Λ_b^0 mass peak. The fitted mass peak is at

5620.93 ± 0.04 MeV.

To view the pK^- mass spectrum, we perform fits, as described above, to the $m(J/\psi\,pK^-)$ distributions in bins of $m(pK^-)$ and extract the signal yields within ± 20 MeV of Λ_b^0 mass peak. The resulting pK^- mass spectrum is shown in Fig. 4.8. A distinct peak is observed in the pK^- invariant mass distribution near 1520 MeV, together with the other resonant and non-resonant structures over the entire kinematical region. The peak corresponds to $\Lambda(1520)$, PDG mass and width of which are 1519.5 ± 1.0 MeV and 15.6 ± 1.0 MeV [1], respectively.

4.3   The $\overline{B}^0 \to J/\psi\,\overline{K}^{*0}(892)$ signal

In this analysis we measure the Λ_b^0 lifetime with respect to the lifetime of $\overline{B}^0$ in the decay $\overline{B}^0 \to J/\psi\,\overline{K}^{*0}(892)$. The same stripping line, trigger and BDT are used to select the $J/\psi\,\pi^+K^-$ candidates. Similar pre-selections are used except for the hadron identification, which are $\mathrm{DLL}(\pi - \mu) > -10$ and $\mathrm{DLL}(\pi - K) > -10$ for pion and $\mathrm{DLL}(K - \pi) > 0$ for kaon. Further selection of ± 100 MeV around the $\overline{K}^{*0}(892)$ mass is applied.

Figure 4.9 shows the $J/\psi\,\pi^+K^-$ distribution. The vertical lines indicate the signal and sideband regions, where the signal region extends to ± 20 MeV around the $\overline{B}^0$ mass peak and the sidebands extend from 60 MeV to 200 MeV below the $\overline{B}^0$ and above the $\overline{B}_s^0$ mass peaks, respectively. The small peak near 5366 MeV results from $\overline{B}_s^0$ decays.

The $\overline{B}^0$ candidate mass distribution can also be polluted by the reflections from $\Lambda_b^0 \to J/\psi\,pK^-$ and $\overline{B}_s^0 \to J/\psi\,K^+K^-$ decays. To determine the size of

the Λ_b^0 and $\overline{B}_s^0$ reflections under the $\overline{B}^0$ signal region we select the mass combinations in the sideband regions and reassign the pion to a proton and a kaon mass hypothesis, respectively. The resulting distributions are shown in Fig. 4.10.

The $m(J/\psi pK^-)$ distribution shows a peak at the Λ_b^0 mass. The $m(J/\psi K^+K^-)$ distribution, on the other hand, shows no peak at $\overline{B}_s^0$ mass and hence not considered further in the analysis. In principle, the reflections from $\overline{B}_s^0 \to J/\psi K^+K^-$ decays should be small, because the production rate times branching fraction is much smaller than $\overline{B}^0 \to J/\psi \overline{K}^{*0}(892)$ and is suppressed by a further factor of ~ 30 from use of the particle ID. We fit the $m(J/\psi pK^-)$ distribution with a Gaussian function for signal and polynomial background. The resulting peak has 1677 ± 78 candidates determined by the fit. Using the simulation of misidentified $\Lambda_b^0 \to J/\psi pK^-$ decays we calculate 545 ± 25 $\Lambda_b^0 \to J/\psi pK^-$ reflection candidates under the $\overline{B}^0$ peak. This number is used as a Gaussian constraint in the mass fit described below.

Figures 4.11 and 4.12 show a fit to the $J/\psi \pi^+K^-$ distribution in linear and log scales, respectively. There are signal peaks at both $\overline{B}^0$ and B_s^0 masses on top of the background. A triple-Gaussian function with common mean is used to fit each signal peak. The fraction and width ratio for the third Gaussian are fixed to that obtained previously in Ref. [11]. The shape of the $B_s^0 \to J/\psi \pi^+K^-$ mass distribution is taken to be the same as that of the signal $\overline{B}^0$ decay. The effective r.m.s. width is 6.4 MeV. An exponential function is used to fit the combinatorial background. The shape of the $\Lambda_b^0 \to J/\psi pK^-$ reflection is taken from simulation, with the yield is Gaussian constrained in the global fit to the expected values. The mass fit gives $330\,787 \pm 626$ signal

37

and $12\,682\pm85$ background candidates together with 544 ± 25 $\Lambda_b^0 \to J/\psi\,pK^-$ reflection candidates within ±20 MeV of the $\overline{B}^0$ mass peak. The fitted mass peaks are at 5281.30 ± 0.01 MeV, and 5368.08 ± 0.37 MeV, for $\overline{B}^0$ and $\overline{B}_s^0$, respectively. The correlation matrix element between the two mass peaks is 0.007.

4.4 Reflections under Λ_b^0 mass peak studied from simulation

To understand the reflections under the $J/\psi\,pK^-$ mass peak, we perform simulations of misidentified $\overline{B}_s^0 \to J/\psi\,K^+K^-$ and $\overline{B}^0 \to J/\psi\,\pi^+K^-$ decays where the K^+ in the former and π^+ in the latter are misidentified as p. We analyze both cases by interpreting the events as $J/\psi\,pK^-$. Then we take each of the candidates in the $J/\psi\,pK^-$ sideband regions and reassign the proton back to a kaon and a pion mass hypotheses, respectively.

Figure 4.13(a) shows the effect of the misidentification of a K^+ as a p, selected in the Λ_b^0 sideband regions, and then reinterpreted as a K^+. The events appear at the $\overline{B}_s^0$ mass as expected. Similarly, Fig. 4.13(b) shows the effect of the misidentification of a π^+ as a p, selected in the Λ_b^0 sideband regions, and then reinterpreted as a π^+. It shows a peak at $\overline{B}^0$ mass as expected. In addition, we start with the $\overline{B}_s^0 \to J/\psi\,K^+K^-$ final state, interpret the K^+ as a π^+ and the π^- as a $\overline{p}$. Then the events in the Λ_b^0 sideband regions are plotted, as shown in Fig. 4.13(c). The distribution shows a large peak near 5230 MeV which is also visible in the misidentified data distribution shown in Fig. 4.4(b). There is a small peak near 5300 MeV. Figure 4.13(d)

shows the distribution from a simulation of $\overline{B}{}^0_s \to J/\psi\,\overline{K}{}^*(892)$ treated as Λ^0_b, being within the sideband region, and then interpreted as $\mu^+\mu^-K^+K^-$. The resulting distribution shows double peaks, one at 5350 MeV and another around 5410 MeV, also visible in Fig. 4.4(a).
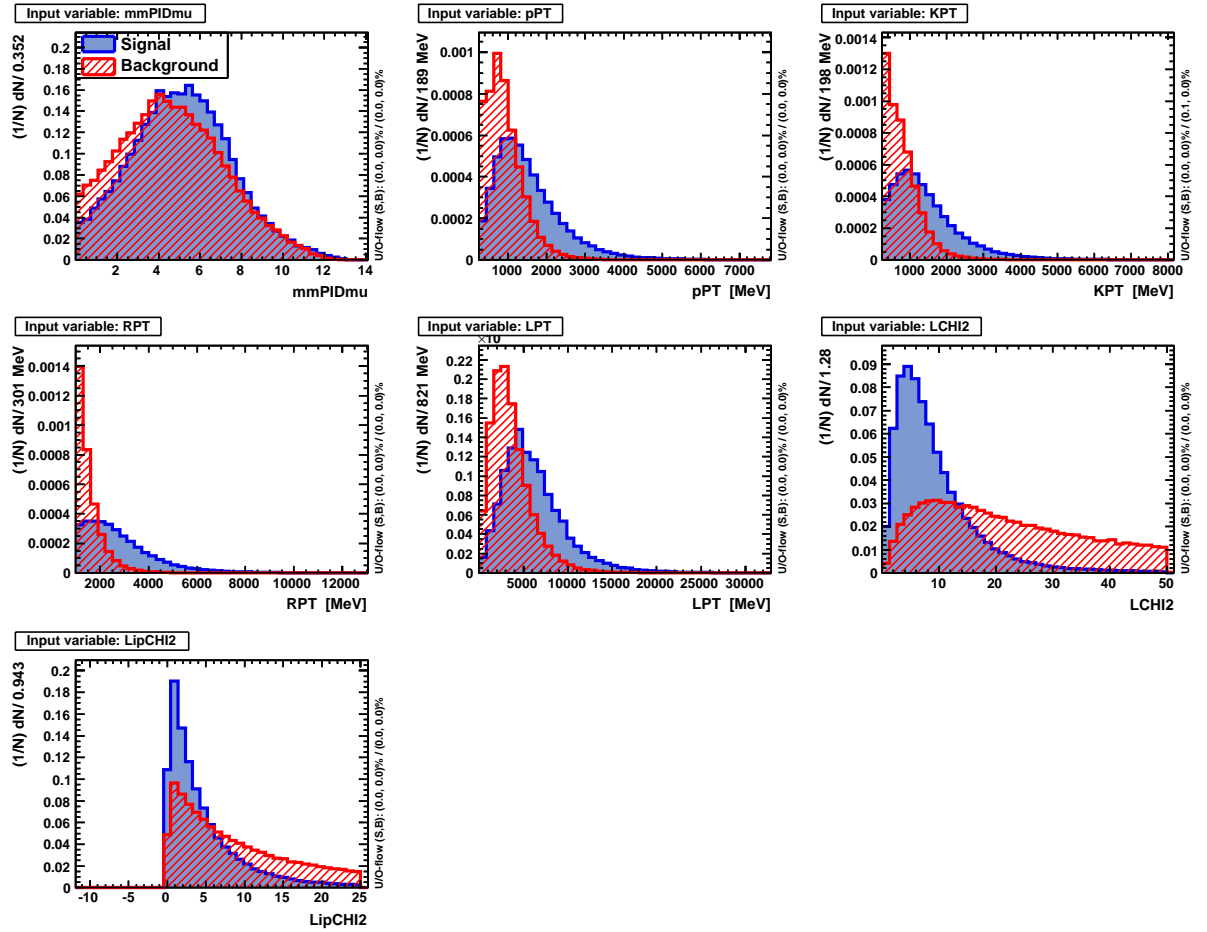
Figure 4.1: Distributions of variables used in BDT.
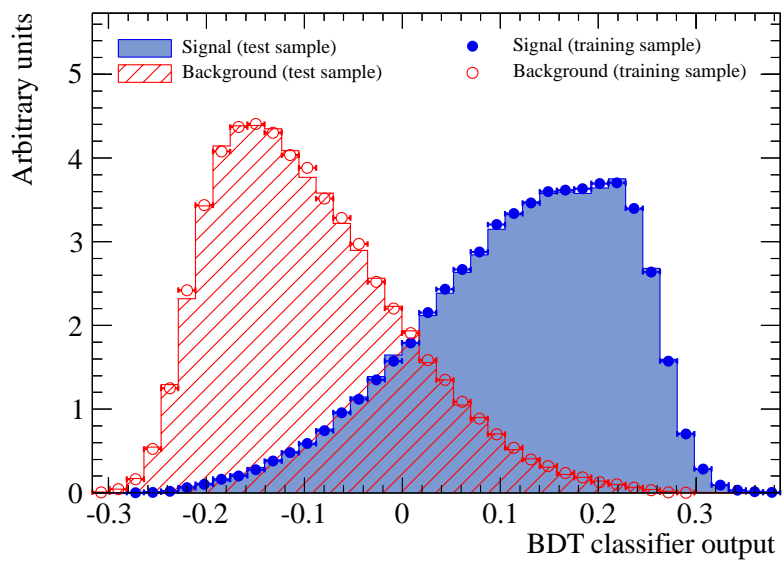
Figure 4.2: BDT distributions for the signal and background.

Figure 4.3: The invariant mass spectrum of $J/\psi\, pK^-$ combinations. The vertical lines indicate the signal (blue long-dashed) and sideband (red dashed) extending from 60 MeV from the peak to the ends of the plot at 200 MeV from the peak.
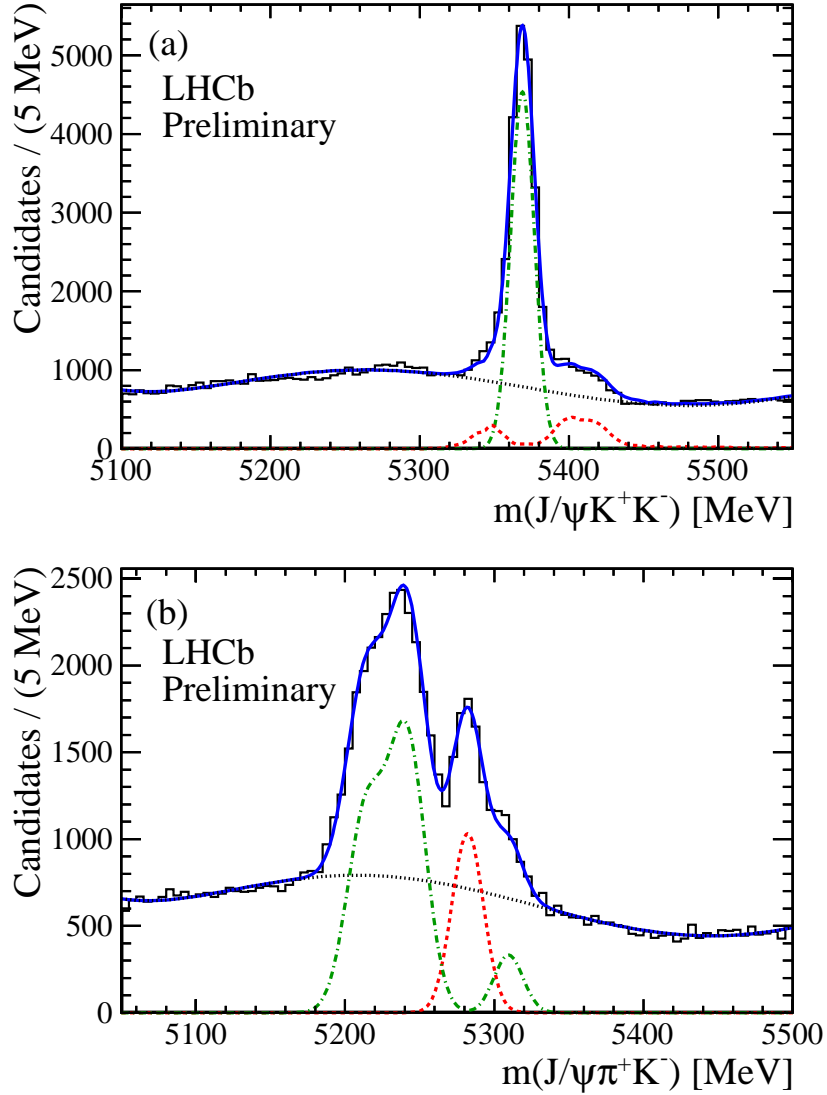
Figure 4.4: The distributions of (a) $m(J/\psi K^+ K^-)$ and (b) $m(J/\psi \pi^+ K^-)$ for $J/\psi\, pK^-$ data candidates in the sideband regions $60 - 200$ MeV on either side of the Λ_b^0 mass peak, reinterpreted as misidentified (a) $\overline{B}_s^0 \rightarrow J/\psi K^+ K^-$ and (b) $\overline{B}^0 \rightarrow J/\psi \pi^+ K^-$ combinations, respectively. The (red) dashed curves show the $\overline{B}^0$ contributions and the (green) dot-dashed curves show $\overline{B}_s^0$ contributions. The (black) dotted curves represent the polynomial background and the (blue) solid curves the total.

43
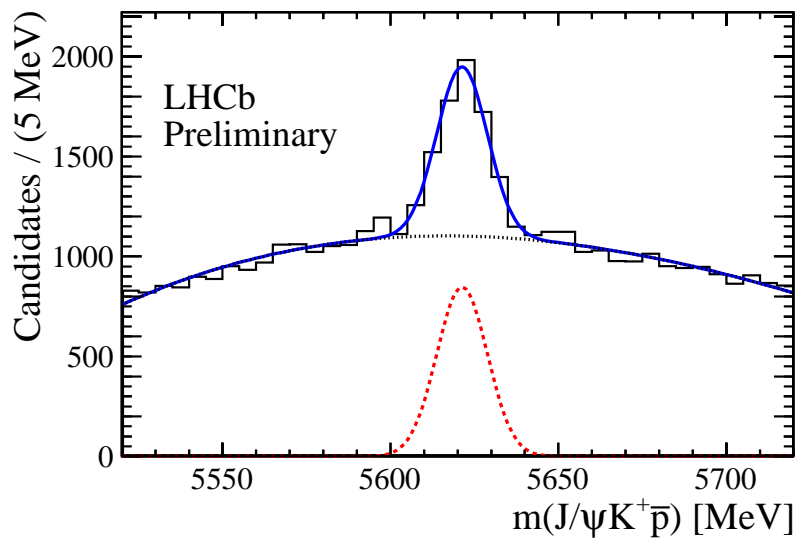
Figure 4.5: The distribution of double misidentification $\Lambda_b^0 \to J/\psi\, p K^-$ with the proton and kaon mass swapped. The (red) dashed curve shows the Λ_b^0 candidates with proton and kaon mass swapped, (black) dotted curve is the polynomial background and (blue) solid curve represents the total.

Figure 4.6: Fit to the invariant mass spectrum of $J/\psi\, pK^-$ combinations. The Λ_b^0 signal is shown by the (magenta) solid curve. The (blue) solid curve shows the total, the (black) dotted line is the combinatorial background, $\overline{B}_s^0 \to J/\psi\, K^+K^-$ and $\overline{B}^0 \to J/\psi\, \pi^+K^-$ reflections are shown with the (violet) dot-dot-dashed and (red) dot-dashed shapes, respectively and the (green) dashed shape represents the double misidentified $J/\psi\, K^+\overline{p}$, where the kaon and proton masses are swapped. The normalized residuals (pull) in each bin are shown below, defined as the differences between the data and the fit divided by the uncertainties on the data. The χ^2/ndf of the fit is 77/53.

Figure 4.7: Fit to the invariant mass spectrum of $J/\psi\,pK^-$ combinations (log plot). The Λ_b^0 signal is shown by the (magenta) solid curve. The (blue) solid curve shows the total, the (black) dotted line is the combinatorial background, $\overline{B}_s^0 \to J/\psi\,K^+K^-$ and $\overline{B}^0 \to J/\psi\,\pi^+K^-$ reflections are shown with the (violet) dot-dot-dashed and (red) dot-dashed shapes, respectively and the (green) dashed shape represents the double misidentified $J/\psi\,K^+\overline{p}$, where the kaon and proton masses are swapped. The normalized residuals (pull) in each bin are shown below, defined as the differences between the data and the fit divided by the uncertainties on the data. The χ^2/ndf of the fit is 77/53.

Figure 4.8: Background subtracted $m(pK^-)$ distribution, obtained by fitting the $m(J/\psi pK^-)$ distribution in bins of $m(pK^-)$.
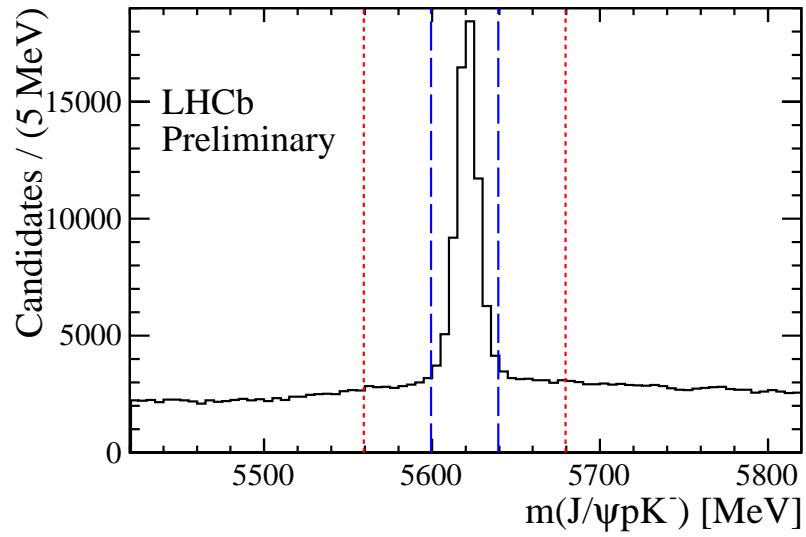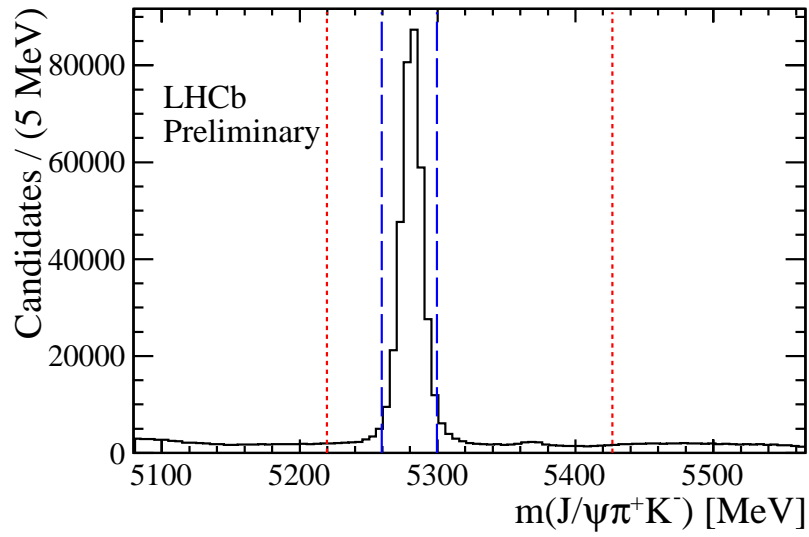
Figure 4.9: The invariant mass spectrum of $J/\psi\,\pi^+K^-$ combinations. The vertical lines indicate the signal (blue long-dashed) and sidebands (red dashed) extending from 60 MeV to 200 MeV below the $\overline{B}^0$ and above the $\overline{B}^0_s$ mass peaks, respectively.
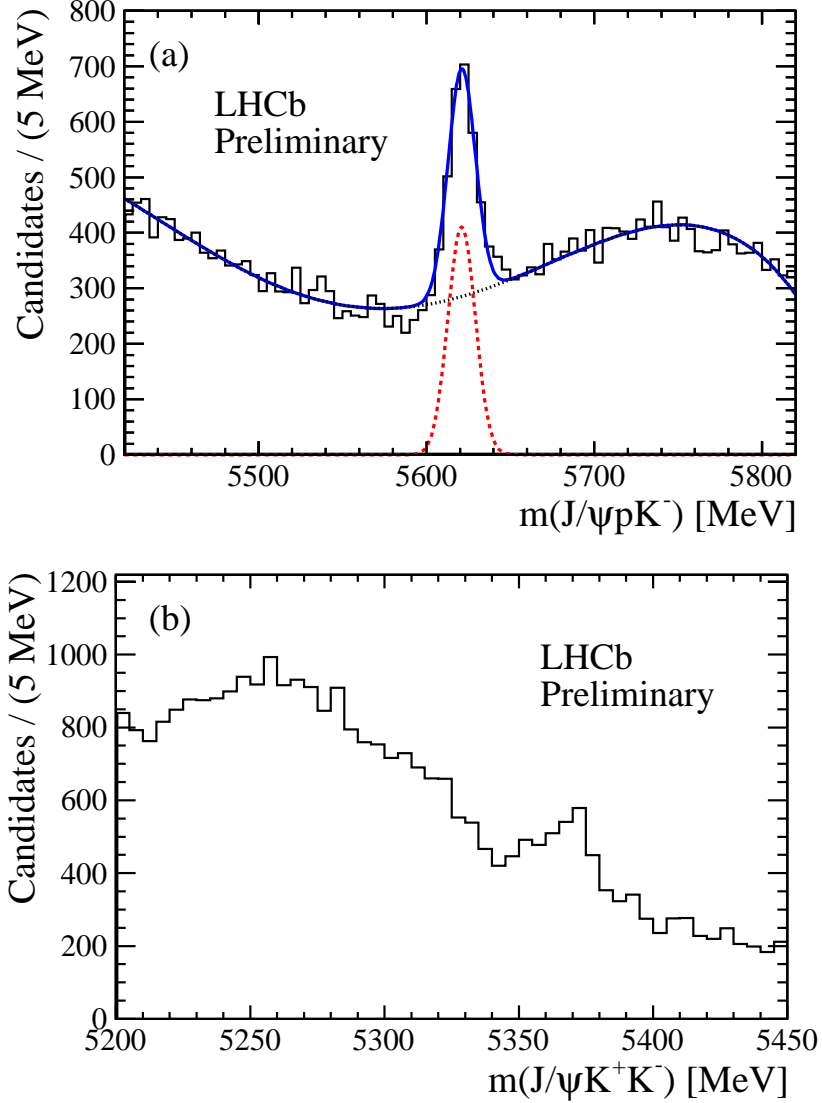
Figure 4.10: The distributions of (a) $m(J/\psi\,pK^-)$ and (b) $m(J/\psi\,K^+K^-)$ for $J/\psi\,\overline{K}^{*0}(892)$ data candidates in the sideband regions, reinterpreted as misidentified $\Lambda_b^0 \to J/\psi\,pK^-$ and $\overline{B}_s^0 \to J/\psi\,K^+K^-$ candidates, respectively. In (a) Λ_b^0 shape is shown by (red) dashed curve, and the background shapes are shown by (black) dotted curve and the (blue) solid curves represent the total.
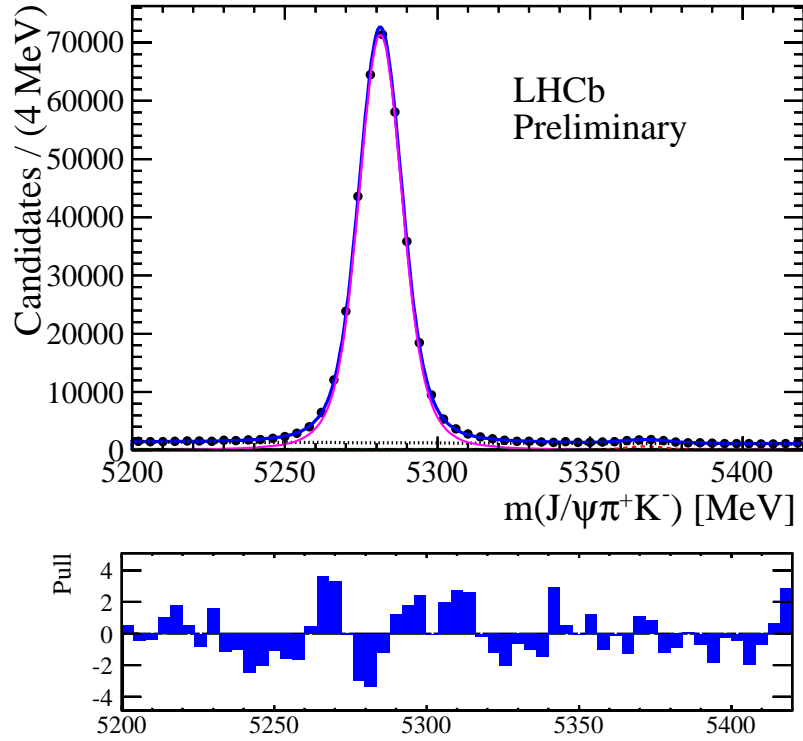
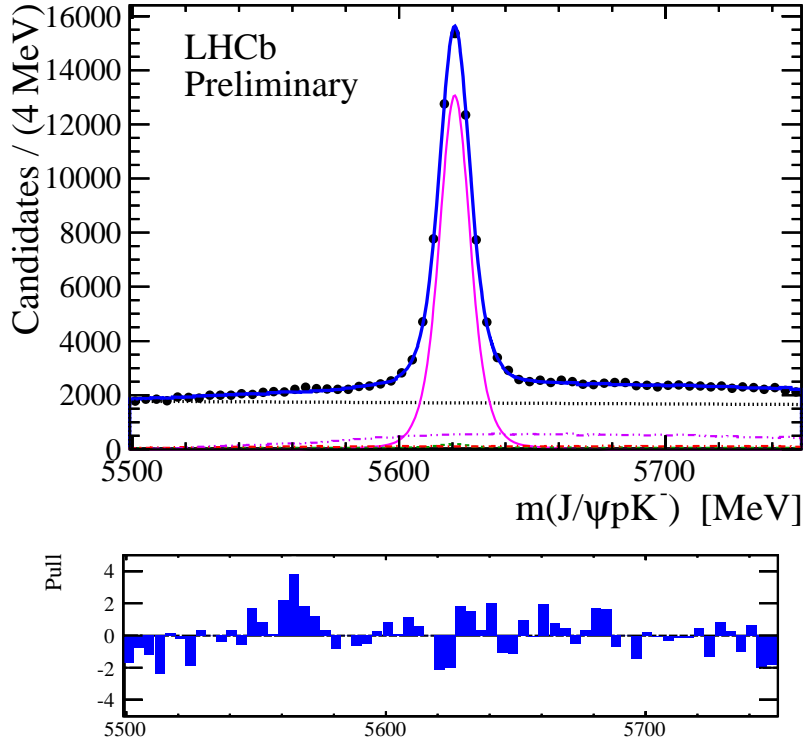Figure 4.11: Fit to the invariant mass spectrum of $J/\psi\,\pi^+K^-$ combinations. The $\bar{B}^0$ signal is shown by the (magenta) solid curve. The (blue) solid curve is the total, the (black) dotted line is the combinatorial background, $B_s^0 \rightarrow J/\psi\,\pi^+K^-$ signal is shown by the (red) dashed curve and (green) dot-dashed shape represents the $\Lambda_b^0 \rightarrow J/\psi\,pK^-$ reflection. The normalized residuals (pull) in each bin are shown below, defined as the differences between the data and the fit divided by the uncertainties on the data. The χ^2/ndf of the fit is 88/45.
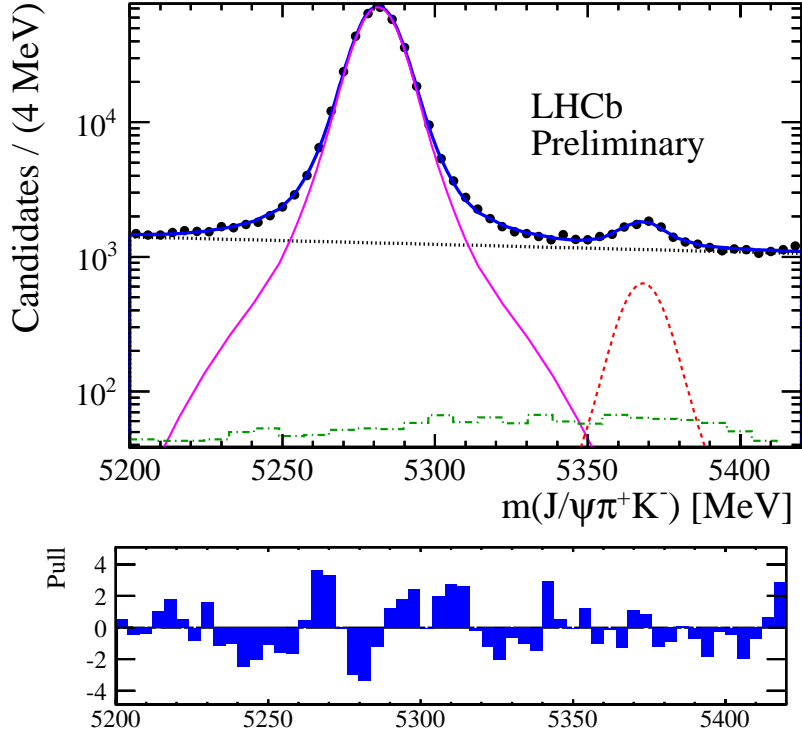
Figure 4.12: Fit to the invariant mass spectrum of $J/\psi \pi^+ K^-$ combinations (log plot). The $\bar{B}^0$ signal is shown by the (magenta) solid curve. The (blue) solid curve is the total, the (black) dotted line is the combinatorial background, $B_s^0 \to J/\psi \pi^+ K^-$ signal is shown by the (red) dashed curve and (green) dot-dashed shape represents the $\Lambda_b^0 \to J/\psi p K^-$ reflection. The normalized residuals (pull) in each bin are shown below, defined as the differences between the data and the fit divided by the uncertainties on the data. The χ^2/ndf of the fit is 88/45.
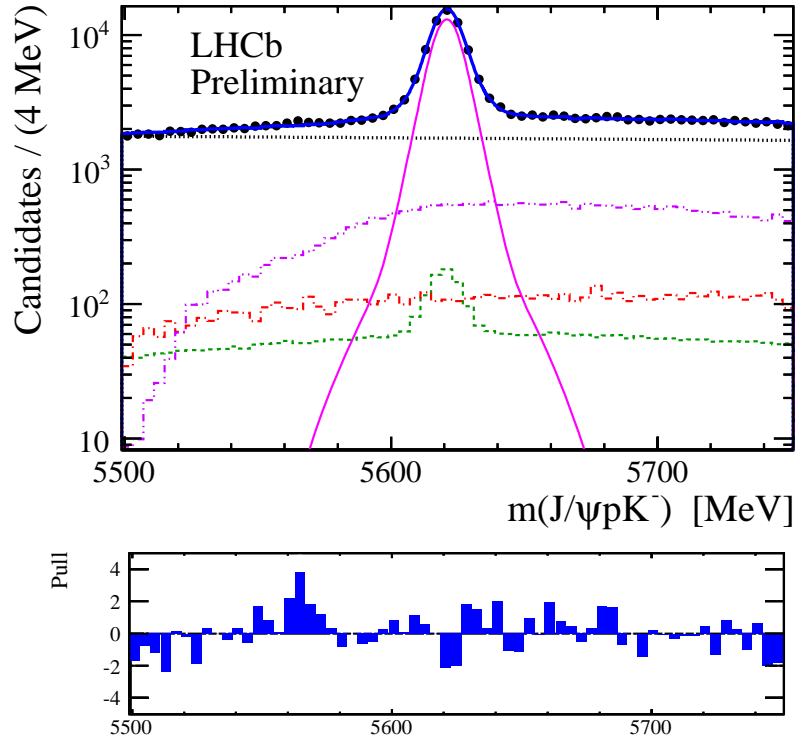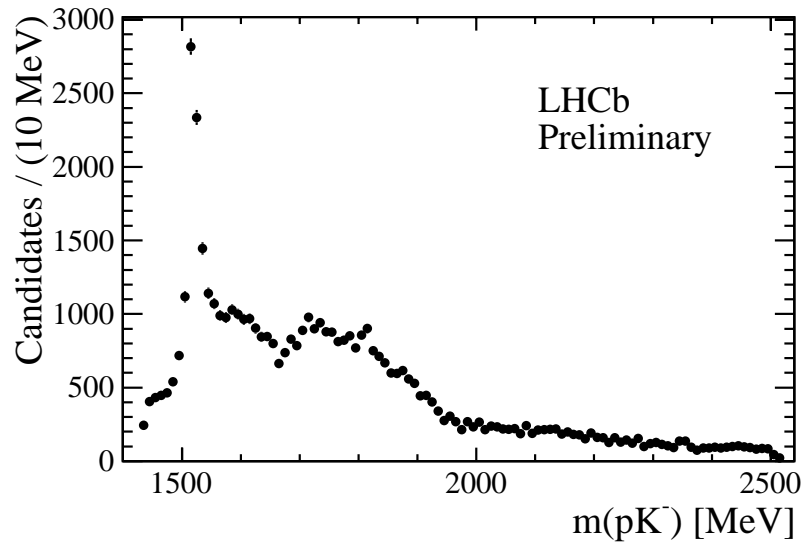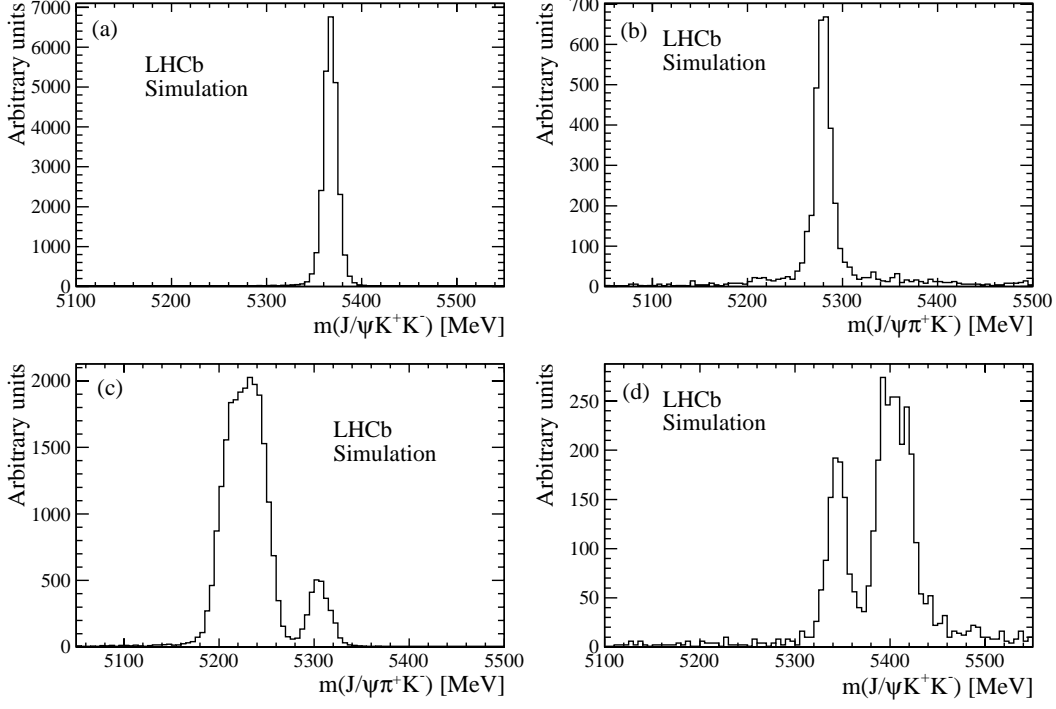
Figure 4.13: (a) For $\overline{B}_s^0 \to \mu^+\mu^- K^+K^-$ events in the J/ψ region, we show the resulting $\overline{B}_s^0$ candidate mass spectrum by misidentifying the K^+ as a p, seeing if the event appears in the Λ_b^0 sideband, and then viewing the $\mu^+\mu^- K^+K^-$ mass spectrum. (b) For $\overline{B}^0 \to \mu^+\mu^-\pi^+K^-$ events in the J/ψ region, we show the resulting $\overline{B}^0$ candidate mass spectrum by misidentifying the π^+ as a p seeing if the event appears in the Λ_b^0 sideband, and then viewing the $J/\psi\pi^+K^-$ mass spectra from $\overline{B}^0$ decay. (c) Again for $\overline{B}_s^0 \to \mu^+\mu^- K^+K^-$ events in the J/ψ region, we show the resulting $\overline{B}^0$ candidate mass spectrum by misidentifying both the K^- as a π^- and the K^+ as a p, checking if the event appears in the Λ_b^0 sideband and plotting the $\mu^+\mu^-\pi^+K^-$ mass. (d) Simulated $\overline{B}_s^0 \to J/\psi\,\overline{K}^*(892)$ treated as Λ_b^0, required to appear in the sideband regions $60 - 200$ MeV from the Λ_b^0 mass peak, and interpreted as $\mu^+\mu^- K^+K^-$, where the two muons are consistent with the J/ψ mass.

52

Chapter 5

Measurement of the Λ_b^0 baryon lifetime

This chapter describes the methodology we used and the details of the measurement of the Λ_b^0 baryon lifetime.

5.1 Analysis method

The decay time, t, is defined as

$$t = m \cdot \frac{\vec{d} \cdot \vec{p}}{|\vec{p}|^2},$$

(5.1)

where m is the reconstructed invariant mass, $\vec{p}$ the momentum and $\vec{d}$ the flight distance vector of the particle between the production and decay vertices. These quantities are obtained from decay tree fitter [42] using the constraint that the direction from the primary vertex to the decay vertex aligns with the B momentum vector. Here, we do not constrain the two muons to the

J/ψ mass in order to avoid systematic biases.

The decay time distribution of $\Lambda_b^0 \rightarrow J/\psi\, pK^-$ can be described by an exponential function convolved with a resolution function, $G(t, \sigma_{\Lambda_b^0})$, multiplied by an acceptance, $A_{\Lambda_b^0}$:

$$F_{\Lambda_b^0}(t) = A_{\Lambda_b^0}(t) \times [e^{-t/\tau_{\Lambda_b^0}} \otimes G(t, \sigma_{\Lambda_b^0})], \tag{5.2}$$

where $\tau_{\Lambda_b^0}$ is the Λ_b^0 lifetime. The ratio of the decay time distributions of $\Lambda_b^0 \rightarrow J/\psi\, pK^-$ and $\overline{B}^0 \rightarrow J/\psi\, \overline{K}^{*0}(892)$ can then be written as

$$R(t) = \frac{A_{\Lambda_b^0}(t) \times [e^{-t/\tau_{\Lambda_b^0}} \otimes G(t, \sigma_{\Lambda_b^0})]}{A_{\overline{B}^0}(t) \times [e^{-t/\tau_{\overline{B}^0}} \otimes G(t, \sigma_{\overline{B}^0})]}. \tag{5.3}$$

The advantage of the method used in the analysis is that the decay time acceptances introduced by the trigger, selection and reconstruction almost cancel in the ratio of the decay time distributions of $\Lambda_b^0 \rightarrow J/\psi\, pK^-$ and $\overline{B}^0 \rightarrow J/\psi\, \overline{K}^{*0}(892)$. In case the acceptances are not equal, a correction can be implemented. Assuming that resolution effects cancels, we are left with a ratio of two exponentials:

$$R(t) = R(0)e^{-t(1/\tau_{\Lambda_b^0} - 1/\tau_{\overline{B}^0})} = R(0)e^{-t\Delta_{\Lambda B}}, \tag{5.4}$$

where $\Delta_{\Lambda B} = 1/\tau_{\Lambda_b^0} - 1/\tau_{\overline{B}^0}$ is the width difference and $R(0)$ is the normalization parameter. The effect of the different decay time resolutions in the two modes are negligible. First order corrections for a decay time dependent acceptance ratio can be taken into account by modifying Eq. (5.4) with a linear function

$$R(t) = R(0)[1 + a \cdot t]e^{-t\Delta_{\Lambda B}}, \tag{5.5}$$

where a represents the slope of the acceptance ratio as a function of decay time.

Small modifications can result if the decay time resolutions of the two modes are significantly different. It has been checked in the previous analysis [11] that the effective decay time resolution is 40 fs for $\Lambda_b^0 \to J/\psi\, pK^-$ and 37 fs for $\overline{B}^0 \to J/\psi\, \overline{K}^{*0}(892)$, which are small enough not to affect the result, as the decay time bin width, used in this analysis is 300 fs.

5.2 The decay time acceptance

The decay time acceptance is defined as the ratio between the reconstructed decay time distribution for selected events and the generated decay time distribution using the generated lifetime (1.424 ps for $\Lambda_b^0 \to J/\psi\, pK^-$ decay and 1.517 ps for $\overline{B}^0 \to J/\psi\, \overline{K}^{*0}(892)$ decay) convolved with the triple-Gaussian decay time resolutions obtained from the simulations. In order to ensure that p and p_{T} distributions of the generated b hadrons are correct, we weight the simulated samples to match the distributions with the corresponding data. The simulations do not model the hadron (pion, kaon and proton) identification efficiencies with sufficient accuracy for our purposes. Therefore we further weight the samples according to the hadron identification efficiencies obtained from $D^{*+} \to \pi^+(D^0 \to K^-\pi^+)$ events for pions and kaons, and $\Lambda \to p\pi^-$ for protons, selected without hadron identification with respect to the simulation [43]. The identification efficiencies are measured in bins of p_{T} and η. Finally, $\Lambda_b^0 \to J/\psi\, pK^-$ sample is weighted using signal yields in bins of $m\,(pK^-)$.

We test the cancellation of acceptance effects using simulated $\Lambda_b^0 \to J/\psi\, pK^-$ and $\overline{B}^0 \to J/\psi\, \overline{K}^{*0}(892)$ events. The decay time acceptances ob-
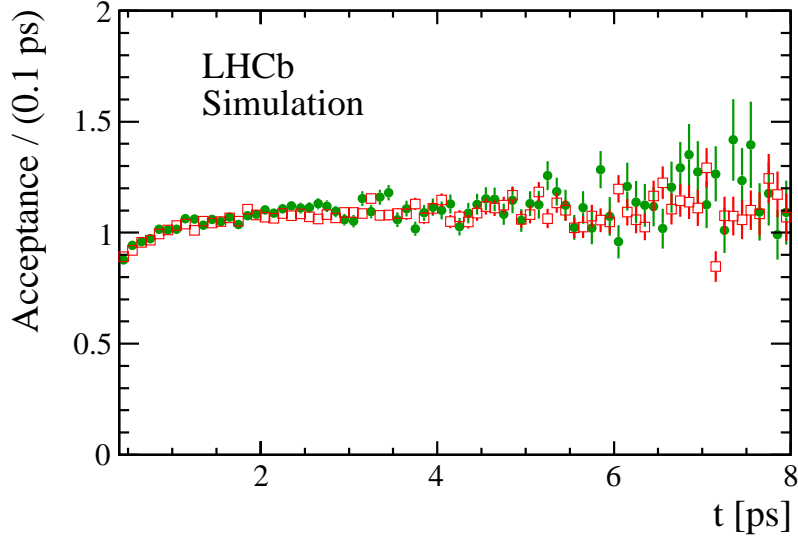
Figure 5.1: The decay time acceptances in simulation for (green points) $\Lambda_b^0 \to J/\psi p K^-$, and (red boxes) $\overline{B}^0 \to J/\psi \overline{K}^{*0}(892)$ decays.

tained from the simulations are shown in Fig. 5.1. The individual acceptances in both cases exhibit the same behaviour. We choose an upper limit cut of 7.0 ps, because the acceptance is poorly determined beyond this value.

The ratio of the decay time acceptances is shown in Fig. 5.2. The acceptance ratio is fitted with a function of the form $C(1+at)$ between 0.4 and 7 ps, with a slope $a = 0.0017 \pm 0.0027$ ps^{-1} and an intercept $C = 1.0050 \pm 0.0061$. Any slope could result from slightly different kinematics between the two decay modes. We use the value of the slope in Eq. 5.5 when fitting the measured decay time ratio.
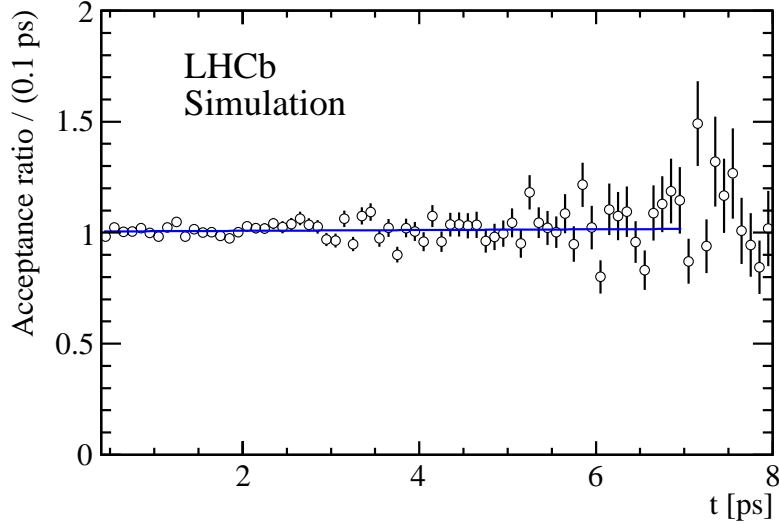
Figure 5.2: Ratio of the decay time acceptances between $\Lambda_b^0 \to J/\psi pK^-$ and $\overline{B}^0 \to J/\psi \overline{K}^{*0}(892)$ decays obtained from simulation. The (blue) line shows the result of the linear fit. The χ^2/ndf of the fit is 91/64.

5.3 Lifetime measurement

In order to determine the $\Lambda_b^0 \to J/\psi pK^-$ lifetime, we determine the yield of b hadrons for both decay modes using unbinned maximum likelihood fits described in Chapter 4 to the b hadron mass distributions in 22 bins of decay time of equal width between 0.4 and 7 ps. The signal and background parameters are held static, obtained by fitting the time-integrated dataset. The resulting distributions are shown in Fig. 5.3. (see also Section 5.4 for the fits in 22 bins of decay time.) The subsequent decay time ratio distribution fitted with the function given in Eq. 5.5 is shown in Fig. 5.4. A χ^2 fit is used with the slope $a = 0.0017 \pm 0.0027$ ps^{-1} fixed, the normalization parameter $R(0)$, and Δ_{AB} are allowed to vary in the fit. The fitted value of the reciprocal
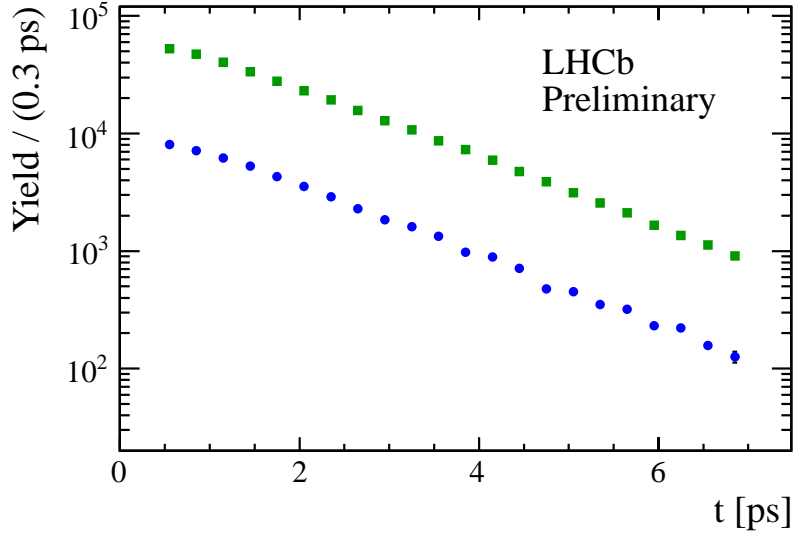
Figure 5.3: Decay time distributions for $\Lambda_b^0 \to J/\psi\, pK^-$ shown as (blue) circles, and $\overline{B}^0 \to J/\psi\, \overline{K}^{*0}(892)$ shown as (green) squares. For most entries the error bars are smaller than the points.

lifetime difference is

$$\Delta_{\Lambda B} = 19.4 \pm 4.7 \pm 3.4 \text{ ns}^{-1}.$$

Whenever two uncertainties are quoted, the first is the statistical and the second systematic. The latter will be discussed in Chapter 6. The χ^2/ndf of the fit is 26/20, with a p-value of 16%. Numerically, the ratio of lifetimes is

$$\frac{\tau_{\Lambda_b^0}}{\tau_{\overline{B}^0}} = \frac{1}{1 + \tau_{\overline{B}^0}\Delta_{\Lambda B}} = 0.971 \pm 0.007 \pm 0.005,$$

where we use the world average value 1.519 ± 0.007 ps [1] for the $\overline{B}^0$ lifetime. Multiplying the lifetime ratio by this value, the lifetime of Λ_b^0 is determined to be

$$\tau_{\Lambda_b^0} = 1.476 \pm 0.010 \pm 0.010 \text{ ps}.$$
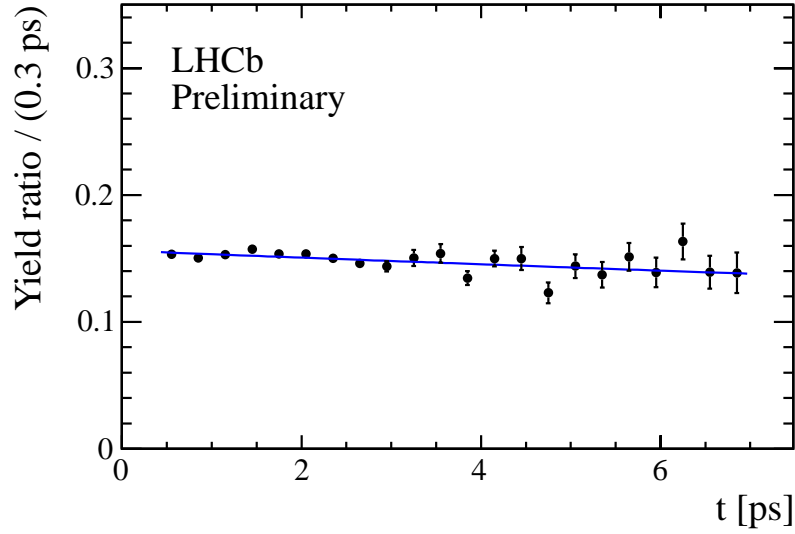
Figure 5.4: Decay time ratio between $\Lambda_b^0 \to J/\psi\, pK^-$ and $\overline{B}^0 \to J/\psi\, \overline{K}^{*0}(892)$ decays, and the fit for $\Delta_{\Lambda B}$ to measure the Λ_b^0 lifetime.

5.4 Mass fits in 22 bins of decay time

The lifetime of Λ_b^0 is measured by fitting the distributions of ratios of signal yields of the decay modes $\Lambda_b^0 \to J/\psi\, pK^-$ and $\overline{B}^0 \to J/\psi\, \overline{K}^{*0}(892)$ in 22 bins of decay time. The signal yields are obtained from unbinned maximum likelihood fit described in Chapter 4. Figures 5.5 and 5.6 show the fits to the $\Lambda_b^0 \to J/\psi\, pK^-$ and $\overline{B}^0 \to J/\psi\, \overline{K}^{*0}(892)$ mass distributions in the 22 bins of decay time.
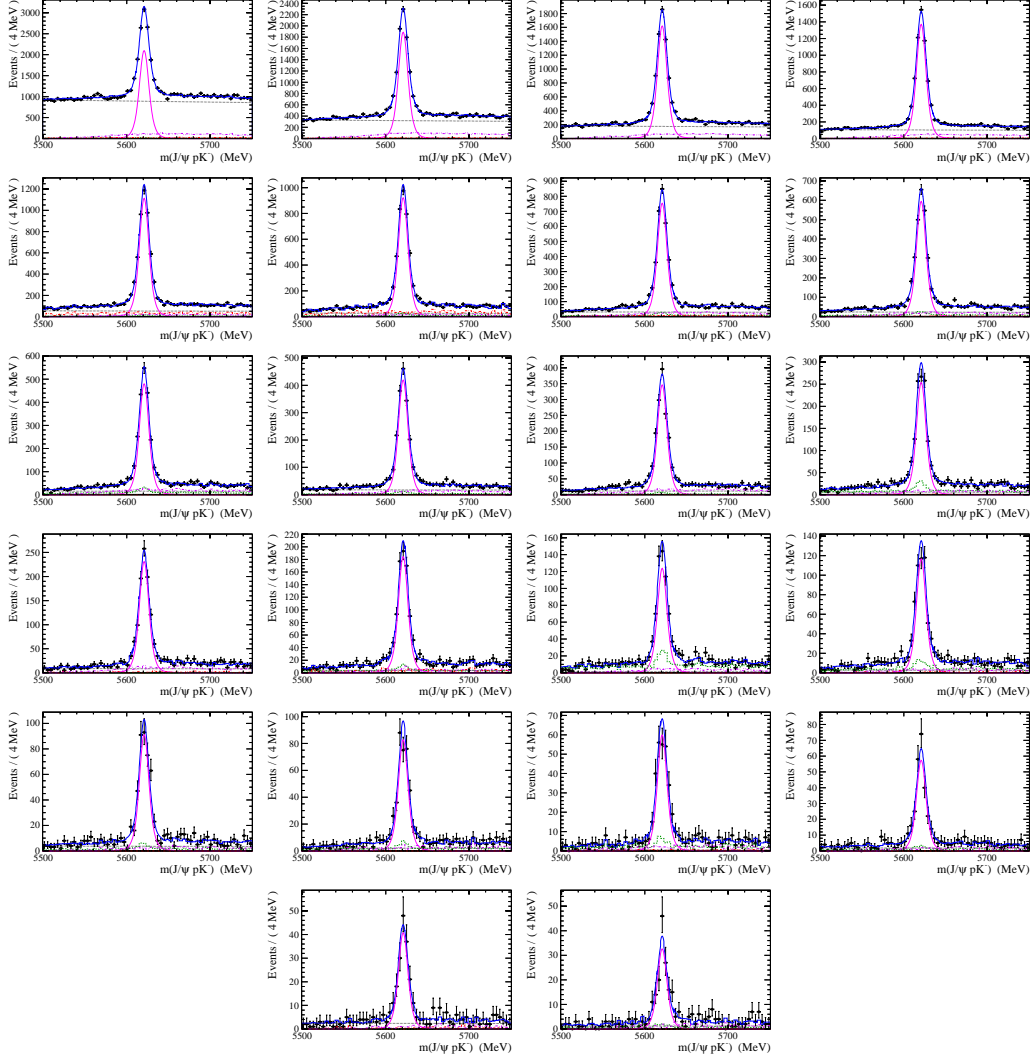
Figure 5.5: Invariant mass distributions of $J/\psi\, pK^-$ events in the 22 bins of decay time from 0.4 to 7 ps. The lowest decay time bin on the top left and the highest decay time bin is on the bottom right. In each plot, the $\Lambda_b^0 \to J/\psi\, pK^-$ signal is shown by the (magenta) solid curve. The (blue) solid curve shows the total, the (black) dotted line is the combinatorial background, $\overline{B}_s^0 \to J/\psi\, K^+K^-$ and $\overline{B}^0 \to J/\psi\, \pi^+K^-$ reflections are shown with the (violet) dot-dot-dashed and (red) dot-dashed shapes, respectively and the (green) dashed shape represents the double misidentified $J/\psi\, K^+\overline{p}$, where the kaon and proton masses are swapped. Here the normalizations on the reflections and double misidentification are allowed to vary.
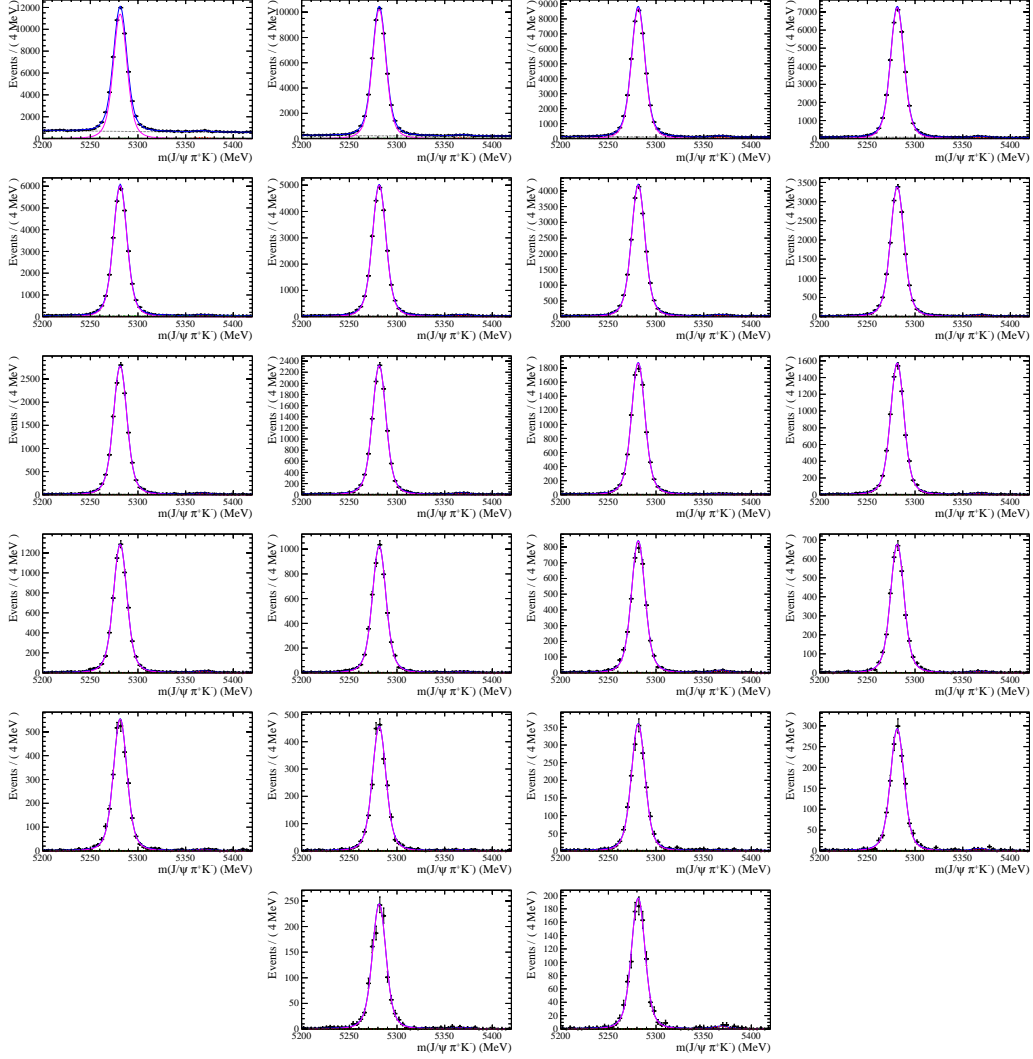
Figure 5.6: Invariant mass distributions of $J/\psi\pi^+K^-$ events in the 22 bins of decay time from 0.4 to 7 ps. The lowest decay time bin on the top left and the highest decay time bin is on the bottom right. In each plot, the $\overline{B}^0 \to J/\psi\,\overline{K}^{*0}(892)$ signal is shown by the (magenta) solid curve. The (blue) solid curve is the total, the (black) dotted line is the combinatorial background, $B_s^0 \to J/\psi\pi^+K^-$ signal is shown by the (red) dashed curve and (green) dot-dashed shape represents the $\Lambda_b^0 \to J/\psi\,pK^-$ reflection. Here the normalizations on the reflections are allowed to vary.

61

Chapter 6

Systematic Uncertainties

This chapter discusses the systematic uncertainties in the measurement of $\Delta_{\Lambda B}$, $\tau_{\Lambda_b^0}/\tau_{\overline{B}^0}$, and $\tau_{\Lambda_b^0}$.

6.1 Systematic uncertainties

Sources of the absolute systematic uncertainties on the $\Delta_{\Lambda B}$, the lifetimes ratio $\tau_{\Lambda_b^0}/\tau_{\overline{B}^0}$ and the Λ_b^0 lifetime are summarized in Table 6.1.

The systematic uncertainty due to the signal model are estimated by comparing the results between the default fit with triple-Gaussian function and the fit with double-Gaussian function, which yields for a value $\Delta_{\Lambda B} = 20.7 \pm 4.8$ ns^{-1}, with a change of 1.3 ns^{-1}, that we assign as the uncertainty. Our signal model shapes are taken independent of lifetime. To assess a systematic uncertainty due to the assumption that the signal function parameters are static in decay time we recalculate the number of data events in each time bin allowing the signal function parameters to vary in

Table 6.1: Absolute systematic uncertainties on the $\Delta_{\Lambda B}$, the lifetimes ratio $\tau_{\Lambda_b^0}/\tau_{\overline{B}^0}$ and the Λ_b^0 lifetime. $\Delta_{\Lambda B}$ is independent of $\overline{B}^0$ lifetime.

Item	$\Delta_{\Lambda B}$ (ns^{-1})	$\tau_{\Lambda_b^0}/\tau_{\overline{B}^0}$	$\tau_{\Lambda_b^0}$ (ps)
Signal shape	1.3	0.0019	0.0029
Background model	0.6	0.0009	0.0014
Acceptance slope	2.7	0.0039	0.0059
Acceptance function	0.1	0.0001	0.0001
Decay time fit range	1.1	0.0016	0.0025
pK helicity	1.0	0.0015	0.0022
$\overline{B}^0$ lifetime	-	0.0001	0.0068
Total	3.4	0.0050	0.0101

each time bin and then redetermine $\Delta_{\Lambda B}$. The change in $\Delta_{\Lambda B}$ is found to be 1.0 ns^{-1}, smaller than the assigned uncertainty due to signal shape and hence no additional uncertainty is assigned.

The uncertainties due to the background parametrization are estimated by replacing the exponential background with a linear function and comparing the difference in the final results. The difference of magnitude 0.6 ns^{-1} for $\Delta_{\Lambda B}$.

The systematic uncertainties due to the acceptance slope are estimated by varying the slope, a, according to its statistical uncertainty. An alternative choice of the acceptance function is also investigated. The systematic uncertainties due to the choice of acceptance function are estimated by comparing the default result with the fit where a second-order polynomial is used to parametrize the acceptance ratio between $\Lambda_b^0 \to J/\psi\, pK^-$ and

$\overline{B}^0 \to J/\psi \, \overline{K}^{*0}(892)$.

There is an uncertainty due to the decay time range used because of the possible change of the acceptance ratio at short decay times. This uncertainty is ascertained by changing the fit range to be $0.7 - 7.0$ ps and using the difference with the baseline fit.

In order to correctly model the acceptance, which can depend on the kinematics of the decay, the $\Lambda_b^0 \to J/\psi \, pK^-$ simulation is weighted according to the $m(pK^-)$ distribution. As a cross-check, we weight the simulation according to the two-dimensional distribution of $m(pK^-)$ and pK^- helicity angle and assign the difference as a systematic uncertainty. Using the PDG value for the $\overline{B}^0$ lifetime, $\tau_{\overline{B}^0} = 1.519 \pm 0.007$ ps [1], as input for the lifetimes ratio and the absolute Λ_b^0 lifetime measurements, requires the propagation of its error as a systematic uncertainty. The total systematic uncertainty is obtained by adding all of the elements in quadrature.

Chapter 7

Conclusions

We determine the ratio of lifetimes of Λ_b^0 and $\overline{B}^0$ as

$$\frac{\tau_{\Lambda_b^0}}{\tau_{B^0}} = 0.971 \pm 0.007 \pm 0.005.$$

This is the most precise measurement to date and consistent with our previously published result [11], with one third of the total dataset used in the current analysis. It shows that the Λ_b^0 and $\overline{B}^0$ lifetimes are indeed equal to within a few percent, as the original advocates of the HQE claimed [3,4,7,9], without any need to find additional corrections. Adding both uncertainties in quadrature, the lifetimes are consistent with being equal at the level of 3.4 standard deviations. Using the world average measured value for the $\overline{B}^0$ lifetime we determine

$$\tau_{\Lambda_b^0} = 1.476 \pm 0.010 \pm 0.010 \text{ ps,}$$

which agrees very well with our previous measurement [11]. Figure. 7.1 shows the current experimental status of the Λ_b^0 baryon lifetime.
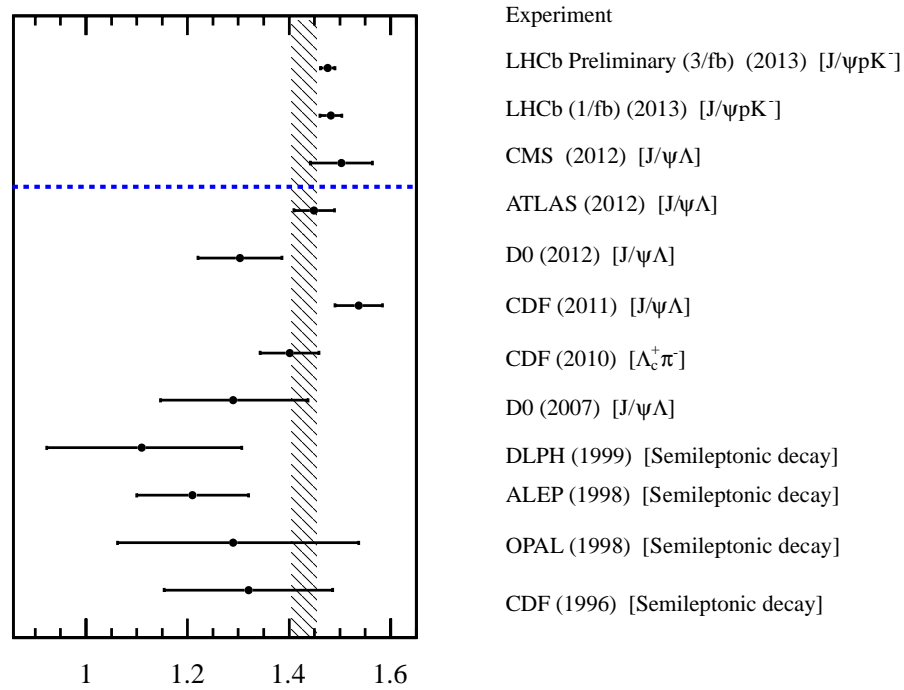
Figure 7.1: Current experimental status of $\tau_{\Lambda_b^0}$. The error bars show the statistical and systematic uncertainties added in quadrature. The band shows the current world average (PDG) [1]. Values above the dashed (blue) line are not included in the world average.

Appendix

Toy simulation

We test our lifetime fitting method in order to insure that there is no fitting biases. To do so, we generate 500 experiments containing signal and combinatorial background with the resolution and acceptance functions included. Triple-Gaussian resolution functions are used, obtained by fitting the simulated decay time resolutions of $\Lambda_b^0 \to J/\psi \, pK^-$ and $\overline{B}^0 \to J/\psi \, \overline{K}^{*0}(892)$ decays, respectively. The acceptance functions are linear, obtained by fitting the acceptances with the first order polynomial. Each of these has the same number of signal and combinatorial background events as the data published previously [11] (approximately one third of the data used in the current analysis). The input lifetimes are taken to same as the previous PDG lifetime [1], $i.e.$, 1.425 ps for Λ_b^0 and 1.519 ps for $\overline{B}^0$. The results are shown in Fig. 2. The fitting method extracts the correct value of Λ_b^0 lifetime without any bias and accurately estimates the statistical uncertainty.
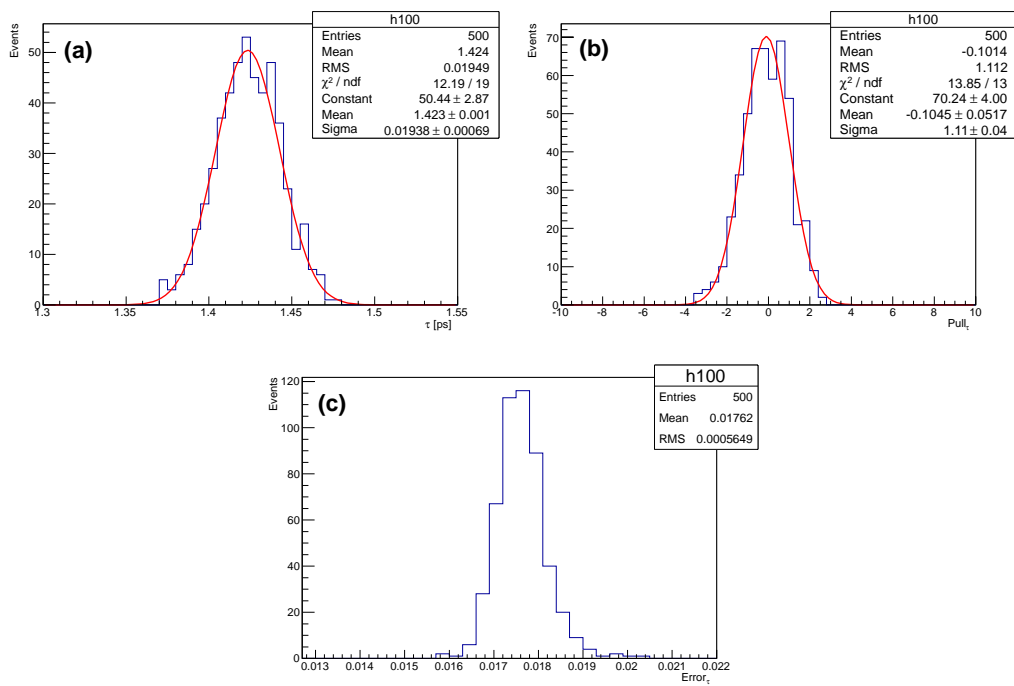
Figure 2: Results of the toy simulation: (a) extracted lifetime distribution, (b) pull distribution and (c) distribution of statistical uncertainty.

Bibliography

[1] Particle Data Group, J. Beringer *et al.*, *Review of Particle Physics*, Phys. Rev. **D86** (2012) 010001.

[2] J. Laiho, E. Lunghi, and R. Van de Water, *Flavor Physics in the LHC era: The Role of the lattice*, PoS **LATTICE2011** (2011) 018, `arXiv:1204.0791`; S. Stone, *New physics from flavour*, `arXiv:1212.6374`.

[3] I. I. Bigi, *The QCD perspective on lifetimes of heavy flavor hadrons*, `arXiv:hep-ph/9508408`; I. I. Bigi, B. Blok, M. A. Shifman, N. Uraltsev, and A. I. Vainshtein, *Nonleptonic decays of beauty hadrons: From phenomenology to theory*, `arXiv:hep-ph/9401298`.

[4] N. Uraltsev, *Heavy quark expansion in beauty and its decays*, `arXiv:hep-ph/9804275`.

[5] M. Neubert, *B decays and the heavy quark expansion*, Adv. Ser. Direct. High Energy Phys. **15** (1998) 239, `arXiv:hep-ph/9702375`.

[6] A. F. Falk, *The CKM matrix and the heavy quark expansion*, `arXiv:hep-ph/0007339`; A. J. Buras, *Climbing NLO and NNLO Summits of Weak Decays*, `arXiv:1102.5650`.

[7] M. A. Shifman and M. Voloshin, *Hierarchy of Lifetimes of Charmed and Beautiful Hadrons*, Sov. Phys. JETP **64** (1986) 698.

[8] H.-Y. Cheng, *A Phenomenological analysis of heavy hadron lifetimes*, Phys. Rev. **D56** (1997) 2783, `arXiv:hep-ph/9704260`; J. L. Rosner, *Enhancement of the Lambda(b) decay rate*, Phys. Lett. **B379** (1996) 267, `arXiv:hep-ph/9602265`.

[9] M. Neubert and C. T. Sachrajda, *Spectator effects in inclusive decays of beauty hadrons*, Nucl. Phys. **B483** (1997) 339, `arXiv:hep-ph/9603202`.

[10] ATLAS Collaboration, G. Aad *et al.*, *Measurement of the Λ_b lifetime and mass in the ATLAS experiment*, Phys. Rev. **D87** (2013), no. 3 032002, `arXiv:1207.2284`; CMS Collaboration, S. Chatrchyan *et al.*, *Measurement of the Λ_b^0 lifetime in pp collisions at $\sqrt{s} = 7$ TeV*, JHEP **07** (2013) 163, `arXiv:1304.7495`; CDF Collaboration, T. Aaltonen *et al.*, *Measurement of b hadron lifetimes in exclusive decays containing a J/ψ in p^- pbar collisions at $\sqrt{s} = 1.96 TeV$*, Phys. Rev. Lett. **106** (2011) 121804, `arXiv:1012.3138`.

[11] LHCb collaboration, R. Aaij *et al.*, *Precision measurement of the Λ_b^0 baryon lifetime*, `arXiv:1307.2476`; Bilas Pal, Sheldon Stone, Liming Zhang, *Measurement of the Λ_b^0 lifetime in the $J/\psi pK^-$ final state*, LHCb-ANA-2013-037.

[12] I. I. Bigi, *The Lifetimes of heavy flavor hadrons: A Case study in quark hadron duality*, `arXiv:hep-ph/0001003`.

[13] K. Wilson and W. Zimmermann, *Operator product expansions and composite field operators in the general framework of quantum field theory*, Communications in Mathematical Physics **24** (1972) 87; G. Buchalla, A. J. Buras, and M. E. Lautenbacher, *Weak decays beyond leading logarithms*, Rev. Mod. Phys. **68** (1996) 1125, `arXiv:hep-ph/9512380`.

[14] N. Uraltsev, *On the problem of boosting nonleptonic b baryon decays*, Phys. Lett. **B376** (1996) 303, `arXiv:hep-ph/9602324`; UKQCD collaboration, M. Di Pierro, C. T. Sachrajda, and C. Michael, *An Exploratory lattice study of spectator effects in inclusive decays of the Lambda(b) baryon*, Phys. Lett. **B468** (1999) 143, `arXiv:hep-lat/9906031`.

[15] M. Battaglia *et al.*, *The CKM matrix and the unitarity triangle. Workshop, CERN, Geneva, Switzerland, 13-16 Feb 2002: Proceedings*, `arXiv:hep-ph/0304132`.

[16] C. Tarantino, *Beauty hadron lifetimes and B meson CP violation parameters from lattice QCD*, Eur. Phys. J. **C33** (2004) S895, `arXiv:hep-ph/0310241`; E. Franco, V. Lubicz, F. Mescia, and C. Tarantino, *Lifetime ratios of beauty hadrons at the next-to-leading order in QCD*, Nucl. Phys. **B633** (2002) 212, `arXiv:hep-ph/0203089`.

[17] T. Ito, M. Matsuda, and Y. Matsui, *New possibility of solving the problem of lifetime ratio tau (Lambda(b)) / tau (B(d))*, Prog. Theor. Phys. **99** (1998) 271, `arXiv:hep-ph/9705402`; F. Gabbiani, A. I. Onishchenko,

and A. A. Petrov, Λ_b^0 *lifetime puzzle in heavy quark expansion*, Phys. Rev. **D68** (2003) 114006, `arXiv:hep-ph/0303235`; F. Gabbiani, A. I. Onishchenko, and A. A. Petrov, *Spectator effects and lifetimes of heavy hadrons*, Phys. Rev. **D70** (2004) 094031, `arXiv:hep-ph/0407004`.

[18] N. Uraltsev, *Topics in the heavy quark expansion*, `arXiv:hep-ph/0010328`.

[19] LHCb collaboration, A. A. Alves Jr. *et al.*, *The LHCb detector at the LHC*, JINST **3** (2008) S08005.

[20] ATLAS collaboration, G. Aad *et al.*, *The ATLAS Experiment at the CERN Large Hadron Collider*, JINST **3** (2008) S08003.

[21] CMS collaboration, S. Chatrchyan *et al.*, *The CMS experiment at the CERN LHC*, JINST **3** (2008) S08004.

[22] ALICE collaboration, K. Aamodt *et al.*, *The ALICE experiment at the CERN LHC*, JINST **3** (2008) S08002.

[23] P. R. Barbosa-Marinho *et al.*, *LHCb VELO (VErtex LOcator): Technical Design Report*. Technical Design Report LHCb. CERN, Geneva, 2001.

[24] J. Gassner, M. Needham, and O. Steinkamp, *Layout and expected performance of the lhcb tt station*, Tech. Rep. LHCb-2003-140, CERN, Geneva, Apr, 2004.

[25] P. R. Barbosa-Marinho *et al.*, *LHCb inner tracker: Technical Design Report*. Technical Design Report LHCb. CERN, Geneva, 2002. revised version number 1 submitted on 2002-11-13 14:14:34.

[26] P. R. Barbosa-Marinho *et al.*, *LHCb outer tracker: Technical Design Report*. Technical Design Report LHCb. CERN, Geneva, 2001.

[27] S. Amato *et al.*, *LHCb magnet: Technical Design Report*. Technical Design Report LHCb. CERN, Geneva, 2000.

[28] S. Amato *et al.*, *LHCb RICH: Technical Design Report*. Technical Design Report LHCb. CERN, Geneva, 2000; M. Adinolfi *et al.*, *Performance of the LHCb RICH detector at the LHC*, Eur. Phys. J. **C73** (2013) 2431, arXiv:1211.6759.

[29] S. Amato *et al.*, *LHCb calorimeters: Technical Design Report*. Technical Design Report LHCb. CERN, Geneva, 2000.

[30] P. R. Barbosa-Marinho *et al.*, *LHCb muon system: Technical Design Report*. Technical Design Report LHCb. CERN, Geneva, 2001; A. A. Alves Jr. *et al.*, *Performance of the LHCb muon system*, JINST **8** (2013) P02022, arXiv:1211.1346; F. Archilli *et al.*, *Performance of the muon identification at LHCb*, arXiv:1306.0249, submitted to JINST.

[31] R. Antunes-Nobrega *et al.*, *LHCb trigger system: Technical Design Report*. Technical Design Report LHCb. CERN, Geneva, 2003. revised version number 1 submitted on 2003-09-24 12:12:22; LHCb collaboration, *HLT description*, http://lhcb-trig.web.cern.ch/lhcb-trig/HLT/HltDescription.htm.

[32] M. Clemencic *et al.*, *Recent developments in the LHCb software framework Gaudi*, J. Phys. Conf. Ser. **219** (2010) 042006; G. Barrand *et al.*, *GAUDI - A software architecture and framework for building HEP data processing applications*, Comput. Phys. Commun. **140** (2001) 45.

[33] M. Clemencic *et al.*, *The LHCb simulation application,* Gauss*: design, evolution and experience*, J. Phys. Conf. Ser. **331** (2011) 032023.

[34] T. Sjöstrand, S. Mrenna, and P. Skands, *PYTHIA 6.4 physics and manual*, JHEP **05** (2006) 026, `arXiv:hep-ph/0603175`.

[35] I. Belyaev *et al.*, *Handling of the generation of primary events in* Gauss, *the LHCb simulation framework*, Nuclear Science Symposium Conference Record (NSS/MIC) **IEEE** (2010) 1155.

[36] D. J. Lange, *The EvtGen particle decay simulation package*, Nucl. Instrum. Meth. **A462** (2001) 152.

[37] P. Golonka and Z. Was, *PHOTOS Monte Carlo: a precision tool for QED corrections in Z and W decays*, Eur. Phys. J. **C45** (2006) 97, `arXiv:hep-ph/0506026`.

[38] Geant4 collaboration, S. Agostinelli *et al.*, *Geant4: a simulation toolkit*, Nucl. Instrum. Meth. **A506** (2003) 250; Geant4 collaboration, J. Allison *et al.*, *Geant4 developments and applications*, IEEE Trans. Nucl. Sci. **53** (2006) 270.

[39] S. Stone and L. Zhang, *Measuring the CP Violating Phase in B(s) Mixing Using $B_s^0 \to J/\psi\, f_0(980)$*, `arXiv:0909.5442`.

[40] L. Breiman, J. H. Friedman, R. A. Olshen, and C. J. Stone, *Classification and regression trees*. Wadsworth international group, Belmont, California, USA, 1984.

[41] LHCb collaboration, R. Aaij *et al.*, *Amplitude analysis and the branching fraction measurement of $\bar{B}_s^0 \to J/\psi K^+ K^-$*, Phys. Rev. **D87** (2013) 072004, arXiv:1302.1213.

[42] W. D. Hulsbergen, *Decay chain fitting with a Kalman filter*, Nucl. Instrum. Meth. **A552** (2005) 566, arXiv:physics/0503191.

[43] LHCb collaboration, *PID Calibration Packages* , https://twiki.cern.ch/twiki/bin/view/LHCb/PIDCalibPackage.

Curriculum Vitae

Bilas Kanti Pal

Education

- **Ph.D.,** Physics (GPA = 4.0)   expected in December 2013

Syracuse University, Syracuse, NY, USA

Advisor: Prof. Sheldon Stone

Dissertation Title: Precision measurement of the Λ_b^0 baryon lifetime

- **MS,** Physics (GPA = 4.0)   2012

Syracuse University, Syracuse, NY, USA

- **DICTP,** High Energy Physics (GPA = 3.62)   2008

The Abdus Salam ICTP, Trieste, Italy

Advisor: Prof. Alexei Yu Smirnov

Dissertation Title: See-saw symmetry

- **M.S.,** Physics (Rank: 1st Class 1st)   2007

University of Dhaka, Dhaka, Bangladesh

Advisor: Prof. Khorshed Ahmed Kabir

Dissertation Title: Neutrino mass and mixing

- **B.Sc.,** Physics (Rank: 1st Class 2nd)   2005

University of Dhaka, Dhaka, Bangladesh

Awards and Honors

- Syracuse University Graduate Fellowship   2012-2013 and 2009-2010
- Henry Levinstein Fellowship   2009
- Research Assistantship, Syracuse University   2010-present
- Teaching Assistantship, Syracuse University   2009, 2010

- ICTP, UNESCO Scholarship and the Travel grant for DICTP   2007-2008
- ICTP, UNESCO Scholarship and the Travel grant for Summer School on Particle Physics   2007
- University First Rank Holder: M.S., University of Dhaka, Bangladesh 2007
- University Second Rank Holder: B.Sc., University of Dhaka, Bangladesh 2005

Teaching

- **Instructor** (Syracuse University)   2009 Summer
PHY 221 - General Physics Laboratory I
- **Teaching Assistant** (Syracuse University)   2010 Spring
AST 104 - Stars, Galaxies and the Universe

Talks

- Measurements of b hadron lifetimes and effective lifetimes at LHCb, DPF 2013 (13-17 November 2013, Santa Cruz, CA)
- ϕ_s measurement at LHCb, Phenomenology 2012 Symposium (7-9 May 2012, University of Pittsburgh)
- LHCb Heavy Flavor Results, 2011 US LHC Users Organization Meeting (3-5 Nov 2011, Argonne National Laboratory)

Publications

- R. Aaij et al. (LHCb Collaboration), "First observation of $\overline{B}^0 \to J/\psi\, K^+ K^-$ and search for $\overline{B}^0 \to J/\psi\, \phi$ decays", Phys. Rev. D. 88, 072005(2013)

- R. Aaij et al. (LHCb Collaboration), "Precision measurement of the Λ_b^0 baryon lifetime;", Phys. Rev. Lett 111,102003(2013).

- R. Aaij et al. (LHCb Collaboration), "Amplitude analysis and branching fraction measurement of $\overline{B}_s^0 \to J/\psi\, K^+ K^-$", Phys. Rev. D 87,072004(2013).

- R. Aaij et al. (LHCb Collaboration), "Analysis of the resonant components in $\overline{B}^0 \to J/\psi\, \pi^+ \pi^-$",Phys. Rev. D 87, 052001 (2013).

- R. Aaij et al. (LHCb Collaboration), "Measurement of the CP violating phase ϕ_s in $\overline{B}_s^0 \to J/\psi\, \pi^+ \pi^-$ Decays", Phys. Letters B 713, 378 (2012).

- R. Aaij et al. (LHCb Collaboration), "Analysis of the resonant components in $\overline{B}_s^0 \to J/\psi\, \pi^+ \pi^-$", Phys. Rev. D 86, 052006 (2012).

- R. Aaij et al. (LHCb Collaboration), "Observation of $\overline{B}_s^0 \to J/\psi\, f_2'(1525)$ in $J/\psi\, K^+ K^-$ final states", Phys. Rev. Lett. 108, 151801 (2012).

- R. Aaij et al. (LHCb Collaboration), "Measurement of the CP violating phase ϕ_s in $\overline{B}_s^0 \to J/\psi\, f_0(980)$ decays", Phys. Letters B 707, 497 (2012).

- R. Aaij et al. (LHCb Collaboration), "First observation of $\overline{B}_s^0 \to J/\psi\, f_0(980)$ decays", Phys. Letters B 698, 115 (2011).

- R. Aaij et al. (LHCb Collaboration), "Measurement of $\sigma(pp \to bbX)$ at 7 TeV in the forward region", Phys. Letters B 694, 209 (2010).